Acta Geotechnica (2024) 19:6217–6237
https://doi.org/10.1007/s11440-023-02220-9

RESEARCH PAPER

A versatile apparatus for assessing the shear behaviour of geotechnical interfaces coupled with imaging and acoustic capabilities

V. L. Gayathri[1] · **Prashanth Vangla**[1] · **Satyam Dey**[1]

Received: 20 May 2023 / Accepted: 20 December 2023

Abstract

This paper presents a versatile interface direct shear test apparatus developed for systematically investigating the shear behaviour of geotechnical interfaces. The apparatus can support the testing of several particle–continuum as well as continuum–continuum interfaces and can also accommodate different configurations of testing, viz. conventional and fixed-box interface shear testing, by a simple rearrangement of the different components. The apparatus facilitates the visualisation and measurement of the deformation of geotextiles under pull-out loading, particle kinematics and the acoustic behaviour of soil–continuum interfaces by accommodating advanced deformation-measurement devices like digital cameras for digital image correlation (DIC) and sensors for acoustic emission (AE). The paper describes the design of all the components of the apparatus and the results of the interface shear tests of different particle–continuum and continuum–continuum interfaces. The repeatability of the test results is verified through multiple tests on the same interface. Results of the interface shear tests indicating the sensitivity of the apparatus for the different modes of testing are also presented. The provisions such as the shear box with a transparent side wall, the moving platform with an interchangeable transparent bottom and the capability to accommodate AE studies facilitated a detailed understanding of various types of interfaces. The DIC results provided insights into the shear zone formation at the dilative interfaces and the deformation of a geotextile under a pull-out load. The AE studies provided a new perspective on the response of particle–continuum interfaces.

Keywords Acoustic emission (AE) · Digital image correlation (DIC) · Geotechnical interfaces · Geotextile pull-out · Interface direct shear test apparatus

1 Introduction

Interfaces, or the region between two materials, are found in many geotechnical engineering systems. These interfaces are potential zones of weakness and instability in the structure, and hence, a systematic understanding of their behaviour is of prime importance for a safe and efficient design, and slope monitoring devices. Interface direct shear test is the most popular and feasible experimental method of determining the shear behaviour and strength parameters of different interfaces. Conventionally, the interface direct shear tests are conducted between soils and different continuum surfaces used in the geotechnical interfaces, such as metals, timber, concrete and geosynthetics [24, 39, 42, 64, 72, 75, 76, 78, 80]. However, recent years have seen many new interfaces in geotechnical engineering applications, such as those between soil and different bio-inspired continuum surfaces and continuum–continuum interfaces [33, 35, 40, 58, 82]. Additionally, several advanced contact and non-contact deformation measurement techniques, such as digital image correlation (DIC) and acoustic emission (AE), are also gaining popularity in the systematic investigation of the shear behaviour of the different interfaces [35, 46, 49, 51, 58, 73, 83, 86].

Several studies have investigated the shear behaviour of different interfaces by modifying the existing direct shear test apparatus to accommodate the continuum material [5, 6, 21, 52, 54, 79]. Over the course of years, several limitations and disadvantages of using such modifications

✉ Prashanth Vangla
prashanth.vangla@civil.iitd.ac.in

[1] Department of Civil Engineering, Indian Institute of Technology Delhi, New Delhi 110016, India

have also come out, such as the effect of the sample size, lack of control on the test parameters and issues such as the rotation of the loading plate and the shear box. Further, adopting the conventional direct shear set-up for the soil–continuum interface shear tests may lead to additional challenges, such as improper clamping of the continuum material due to spatial constraint, slippage of the continuum material, introduction of additional shear planes when the continuum materials are glued, and the eccentricity in the plane of measurement of the shear forces when the thickness of the continuum material changes. Lee & Manjunath [50] also indicate that using the conventional direct shear test apparatus for soil–continuum interface shear studies in which the continuum material is placed between the soil in the two shear boxes may induce additional sagging of the continuum material, which may further aggravate the non-uniform stresses and strains at the shear plane. A few researchers have also developed new interface shear test apparatuses that can serve specific purposes [1, 29]. However, a dedicated interface shear test apparatus that can accommodate different interfaces, test configurations, modes of testing and advanced instrumentation is essential for a thorough and systematic understanding of their interface shear behaviour. Such a versatile apparatus can also help in the visualisation and analysis of the different phenomena happening at the interface during the shearing process by accommodating advanced non-contact deformation measurement techniques such as DIC and AE and can pave the way for reliable and novel insights into different aspects of the interface shear behaviour.

This paper describes the design and fabrication of a versatile interface direct shear test apparatus that can support the testing of several particle–continuum as well as continuum–continuum interfaces. The apparatus is designed to facilitate different testing configurations, viz. conventional and fixed-box interface shear testing by a simple rearrangement of the different components. Furthermore, the apparatus accommodates advanced deformation-measurement devices like digital cameras for DIC and AE sensors. The paper describes the design of all the components of the apparatus, and the performance and accuracy of the apparatus are validated through interface shear tests on different non-dilative, dilative and continuum–continuum interfaces. Additionally, the advantages of the novel facilities and advanced instrumentation, including digital cameras and AE sensors, are also demonstrated through a series of shear tests on different interfaces.

2 Description of the apparatus

The apparatus was designed by abiding by the general guidelines and suggestions in ASTM D5321/D5321M-21[15]. Figure 1 presents the schematic 2D cross section of the apparatus. Figure 1a presents the conventional interface shear test set-up and Fig. 1b shows the fixed-box interface shear test set-up. The apparatus mainly consists of a shear box in which the soil or soft rock sample can be kept and a movable platform where the continuum material can be fastened or clamped. The shear box and the movable platform are assembled on a table. The shear box (1) has three walls made of brass and a fourth transparent side wall made of acrylic to facilitate image-capturing of the sample during shearing and also has rounded corners to reduce undesirable stress concentrations. Two shear boxes of square shape, one with 100 mm (length) X 100 mm (width) X 75 mm (height) internal dimensions and the other with internal dimensions of 150 mm (length) X 150 mm (width) X 95 mm (height), with associated shear and load plates, were designed to facilitate different sample to grain-size ratio combinations. Figure 2a shows a 3D image of the shear box and the associated components. The shear box with the sample is kept over the movable platform (2), which has a rectangular cross section with dimensions of 400 mm (length) X 300 mm (width), the 3D view of which is shown in Fig. 2b. The dimensions of the platform allow the clamping of different sizes of the continuum materials onto it for both 100 mm X 100 mm and 150 mm X 150 mm shear boxes and facilitate a continuous shearing of up to 60 mm with a constant area of shearing. The dimensions of the platform also facilitate the easy assemblage of the acoustic emission sensors at any desired location without any disturbance to the interface shearing. The platform and the shear box are assembled on top of a table through a frictionless linear bearing support system (3). The platform is movable in both forward and backward directions, using a worm-drive stepper motor (4). The normal load on the samples is applied with dead loads using a loading frame connected to a lever arm and vertical support rods. One of the vertical supporting rods parallel to the transparent side of the acrylic side of the shear box is made rectangular (5) to facilitate image capturing during the shear tests. The apparatus is equipped with load cells for horizontal (6) and vertical (7) load measurements and linear variable displacement transducers (LVDT) for displacement measurements in the horizontal (8) and vertical (9) directions. ASTM D5321/D5321M-21[15] states that an eccentric application or measurement of the shear force may give inaccurate results, and hence, it is essential to ensure that the line of action of the shear force is collinear with the shearing plane interface. Such eccentric loading

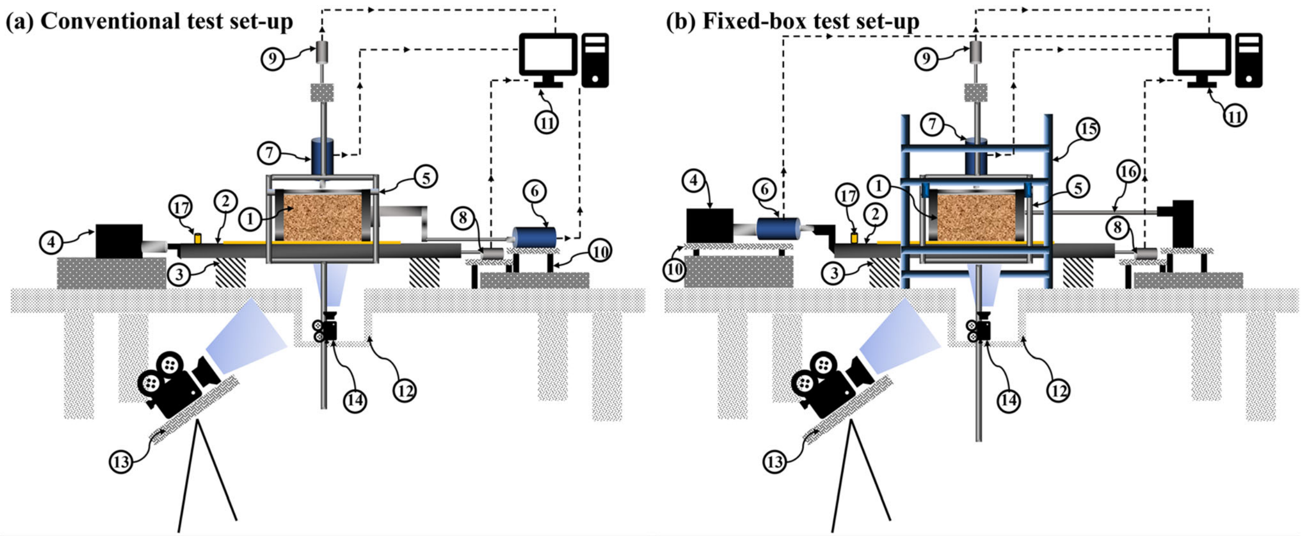

1. shear box with the soil sample, 2. movable platform with the clamped continuum surface, 3. frictionless supports with ball bearing, 4. worm-drive stepper motor, 5. rectangular loading frame to facilitate image-capturing load cell for horizontal force measurement, 6. load cell for horizontal force measurement, 7. load cell for vertical force measurement, 8. LVDT for horizontal displacement measurement, 9. LVDT for vertical displacement measurement, 10. adjustable platform for the horizontal load cell, 11. data acquisition system, 12. table with slot arrangement for camera placement, 13. CMOS sensor camera for image-capturing from the front, 14. CMOS sensor camera for image-capturing from the bottom, 15. vertical support system to facilitate fixed-box condition, 16. additional rod support to prevent box rotation, 17. AE sensor.

Fig. 1 Schematic representation of the interface shear apparatus for **a** conventional test configuration, and **b** fixed-box test configuration

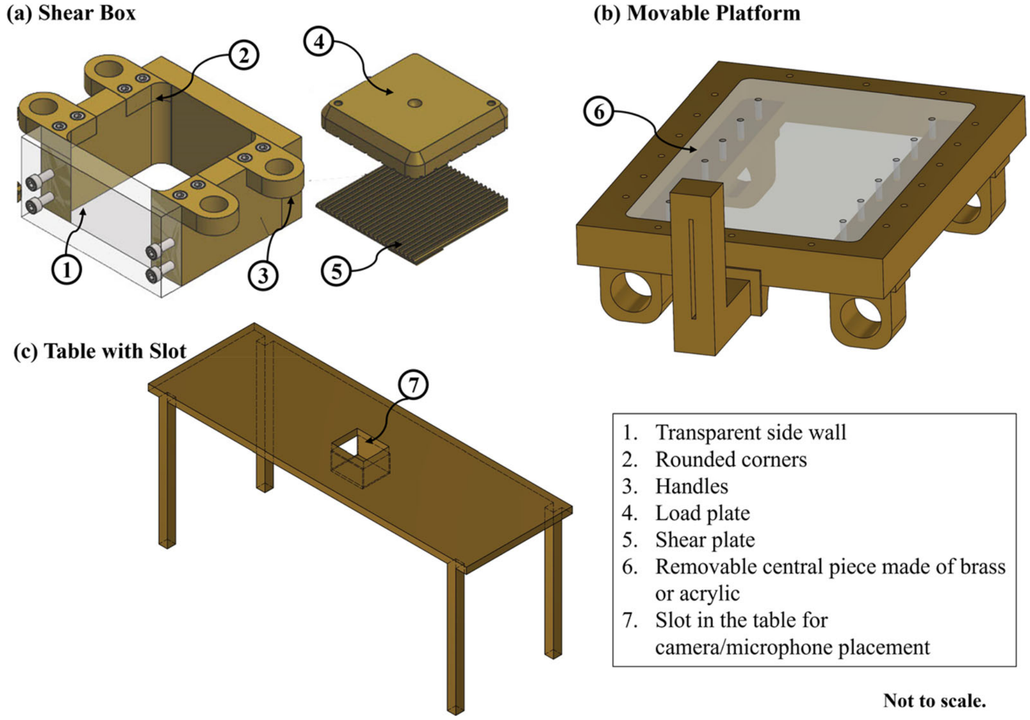

1. Transparent side wall
2. Rounded corners
3. Handles
4. Load plate
5. Shear plate
6. Removable central piece made of brass or acrylic
7. Slot in the table for camera/microphone placement

Not to scale.

Fig. 2 3D views of **a** shear box, **b** movable platform, and **c** table with slot

may occur when continuum materials of different thicknesses are clamped onto the platform (2). Hence, the horizontal load cell (6) rests on a sturdy platform (10) whose elevation can be adjusted upwards and downwards using a simple rotating rod arrangement. Several types of clamps are also designed that allow the clamping and testing of the different interfaces. The apparatus is equipped with a data acquisition system (11) for continuous monitoring and recording of the test data. More details on the instrumentation and the fixed-box test set-up are given in the subsequent sections.

2.1 Conventional and fixed-box configurations

The conventional interface shear tests, in which the load plate rests freely on the soil sample, may cause rotation of the soil sample during shearing, which in turn leads to non-uniform stress concentrations in the sample [27, 61], and may cause erroneous results. Jewell and Wroth [44] and Jewell [43] observed that the rotation of the load plate, and the relative rotation of the shear box, can be minimised by fixing it to the walls of the shear box. Keeping this in view, the apparatus has been designed to accommodate both conventional and fixed-box configurations of the interface shear tests by a simple rearrangement of the components of the apparatus.

Additional fixity elements and supporting rods were designed for rearranging the apparatus to the fixed-box configuration. Firstly, the shear boxes were designed with additional handles, as shown in Fig. 2a, which are used to attach the shear box to robust vertical supporting rods (15). Specially designed Z-shaped brackets, nut and bolt systems, and an additional horizontal rod (16) connected to an immovable stand, are used to hold the shear box firmly in position to prevent its rotation while shearing, as shown in Fig. 3. As the shear box is fixed, the horizontal load cell is shifted to the opposite side and connected to the worm-drive stepper motor and the movable platform, as shown in Fig. 1b so that the shear data at the interface plane are recorded.

2.2 Image analysis

The apparatus has provisions to accommodate image–capturing of the interfaces for various purposes, which are listed as follows:

- The shear box has one transparent wall made of acrylic, as shown in Fig. 2a, so that images of the soil–continuum interfaces can be captured from the side. This is particularly advantageous when the visualisation and analysis of the soil–continuum interface shear zones are desired. For this purpose, the vertical rod of the loading frame is made rectangular, as shown schematically in Fig. 1, so that the images can be captured unobstructed.
- The movable platform has a central brass piece, which is removable and can be replaced by a transparent acrylic sheet, as shown in Fig. 2b. The table has a slot arrangement, as shown in Fig. 2c, under which a camera can be attached to capture images using a custom-made camera holder. Images from the bottom

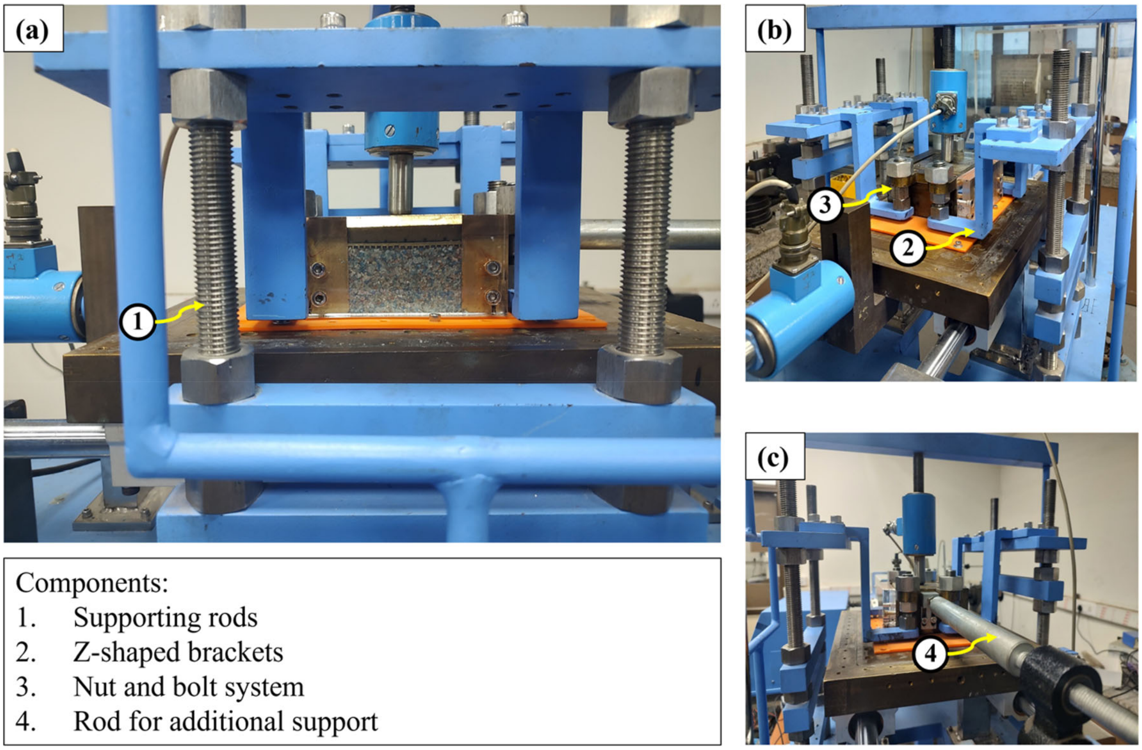

Fig. 3 The details of the fixed box configuration, **a** front view of the assembled box, **b** side-view showing the custom-made Z-shaped brackets and nut and bolt system, and **c** rod for additional support

of the sample can aid in the visualisation and analysis of particle kinematics during interface shearing, as shown and explained in detail in Kandpal and Vangla [45]. It is also beneficial for the analysis and visualisation of the deformation behaviour of the continuum materials like geotextiles under pull-out load, using DIC, which provides the advantages of the non-contact deformation measurement technique and eliminates the need for additional deformation sensors.

These provisions make the apparatus versatile and fully functional for gaining novel insights into the shear mechanisms of different geotechnical interfaces, which are further discussed in a later section.

2.3 Instrumentation and data acquisition

The apparatus is equipped with an eight-channel data acquisition cum data logging system. The data acquisition system has a specially designed built-in software and hardware control to operate the apparatus at the desired shear displacement rate and direction. The horizontal load cell is analogue and has a capacity of 5 kN and has full-scale reading for horizontal pushing (forward shear direction) and pulling (backward shear) loads, while the vertical analogue load cell has a capacity of 10 kN capacity with full-scale reading for the normal vertical load. Both the load cells have an accuracy of 1 N. The horizontal LVDT can measure up to 60 mm and has an accuracy of 0.01 mm, while the vertical LVDT has a stroke of 20 mm, with 0.01 mm accuracy. The worm-drive stepper motor can facilitate a range of horizontal pulling/pushing speeds from 0.05 to 10 mm/min.

The set-up also includes cameras and other accessories for image capturing and analysis. Two machine vision cameras with CMOS sensors (Sony IMX26) of 9 MP and 5 MP resolutions on which machine vision lenses can be attached. The cameras are capable of recording both image and video files. A machine vision lens of 50 mm focal length is found to be appropriate for image capturing from the side of the shear box, while a machine vision lens of 12 mm focal length is required to appropriately capture images from the bottom of the platform. The Baumer camera explorer software is used to capture the images at the desired frequency in grey-scale format. The images captured using these cameras and lenses were found to have a resolution of 25 pixels/mm. A machine vision lighting source was also used for the uniform lighting of the test area during image capturing.

Table 1 Specifications of the two sensors

Sensor data	AE sensor
Type	Low power integral preamplifier cylindrical piezoelectric sensor
Operating frequency range	10–100 kHz resonant frequency: 50 kHz
Temperature range	− 35 to + 80 °C
Sensitivity	101 dB
Sampling frequency used	1 MHz

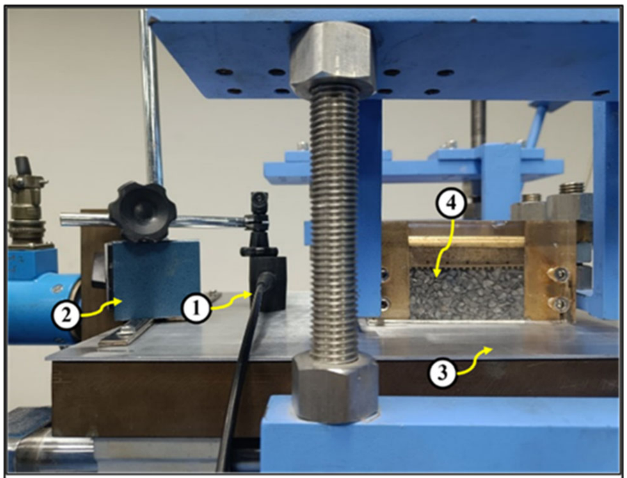

1. AE sensor, 2. Magnetic holder, 3. Continuum material, 4. Granular material

Fig. 4 The arrangement of the AE sensor using a modified magnetic holder

The shearing at the soil–metal interface generates elastic/stress waves in the metal plate, referred to as a Lamb wave [48] in a thin metal plate. These waves were captured by the AE sensor (the specifications are presented in Table 1) placed on the top of the metal plate using a magnetic holder, as shown in Fig. 4, which is connected to a high-sampling data acquisition system (DAQ). The stress waves have a critical frequency range of 20–100 kHz; beyond this limit, the results are inconsistent, which was verified through preliminary investigation and also reported in the literature [71]. Thus, a sampling frequency of 1 MHz is used to reconstruct a 100 kHz wave without distortion digitally, which is five times the Nyquist frequency, the minimum sampling frequency required to avoid aliasing. The apparatus and acoustic emission DAQs are synchronised to record the interface shear and acoustic emission responses during the test simultaneously.

3 Materials and methods

3.1 Particulate materials (soil)

The interface shear tests in the study are conducted using different soils. A specific size fraction, passing through a 2 mm sieve and retaining on 1 mm, is scalped from the quarry sand (QS) and glass beads (GB) and oven-dried to remove any moisture present. Scalping of the sand particles was carried out to have better control over the size of the particles and the gradation, as shown in different studies [20, 32, 78–80], and to conform to the recommendations in ASTM D3080 [10]. Both sands are classified as poorly graded sand (SP) with a mean particle size (D_{50}) of 1.5 mm. A third sand (AS) of sizes ranging from 2 to 4 mm is used for the AE and geotextile pull-out tests. The shape parameters of the sands are determined by an image-based technique, suggested by Vangla et al. [81]. The average roundness (R) and average sphericity (S_{wl}) of QS are found to be 0.21 and 0.68, respectively, while that of AS is 0.80 and 0.59. The GB have an R of 0.99 and S_{wl} of 0.96. QS is thus characterised as angular, while AS is sub-angular and GB are well-rounded, as per the criteria suggested by Powers [65]. The fourth soil (CS) was obtained from a proposed landfill site and was classified as clay of low to medium plasticity (CL). All soils were classified as per United Soil Classification System (USCS) [9]. The angle of internal friction (φ) of the soils was found from the Mohr–Coulomb failure envelope described as

$$\tau_s = c + \sigma_n * \tan(\varphi) \tag{1}$$

where τ_s is the shear strength of the soil, c is the cohesion intercept, and σ_n is the applied normal stress. The relevant properties of the particulate materials, determined as per the ASTM standards, are given in Table 2.

Table 2 Properties of the particulate material (soil)

Soil	Property	Value			Test method
		QS	GB	AS	
Sand	Specific gravity (G)	2.69	2.53	2.65	ASTM D854 [8]
	Max. dry unit weight, kN/m^3 ($g_{\text{d-max}}$)	15.9	13.7	15.1	ASTM D4253-16 [11]
	Min. dry unit weight, kN/m^3 ($g_{\text{d-min}}$)	13.8	13.2	13.3	ASTM D4254-16 [12]
	Max. void ratio ($e_{\max}$)	0.92	0.88	0.95	ASTM D4254-16 [12]
	Min. void ratio ($e_{\min}$)	0.66	0.81	0.72	ASTM D4253-16 [11]
	Angle of internal friction, deg (φ)	46.4	32.1	46.6	ASTM D3080 [10]
	Cohesion, kPa (c)	0	0	0	
Clay (CS)	Liquid limit (%)	37			ASTM D4318-17 [13]
	Plastic limit (%)	15.5			
	Optimum moisture content (%)	15.6			ASTM D698-12 [7]
	Maximum dry density, g_d (kN/m^3)	17.85			
	Angle of internal friction, deg (φ)	16.1			ASTM D3080 [10]
	Cohesion, kPa (c)	21			

3.2 Continuum materials

Several continuum materials, as shown in Fig. 5, were used in the study to demonstrate the different capabilities of the apparatus. A fused filament fabrication (FFF) 3D printer was used to fabricate planar continuum materials with different surface textures using polylactic acid (PLA) polymer. The fused filament fabrication (FFF) method of 3D printing was chosen as it is one of the most widely used methods of 3D printing due to its ease of usage, printing flexibility, and cost-effectiveness. FFF involves melting thermoplastic material and depositing it in layers onto a heated surface to produce 3D models by means of two extruders that move and accurately dispense the molten filaments onto the heated bed in thin layers [70, 85]. The 3D-printed continuum surfaces include a plain continuum surface (termed PLA in the study) for the non-dilative interfaces, a continuum surface with ribs of height 1 mm and width 1.5 mm, spaced at 7 mm intervals (PLA_R) for the dilative interfaces, and a snakeskin-inspired patterned continuum surface (PLA_S) to study its shear behaviour with Plaster of Paris (PoP) blocks. These 3D-printed continuum surfaces have outer dimensions of 180 mm (length) X 170 mm (width) X 1.5 mm (thickness) and consist of a patterned area of 180 mm (length) X 136 mm (width) for PLA_R and PLA_S. The interface shear tests on non-dilative and dilative tests were also studied using factory-made HDPE geomembranes of 1.5 mm thickness, one of which was smooth (GM), and the other was patterned (GM_P). A non-woven geotextile (GTx) was selected to study its shear behaviour and deformations under pull-out conditions. A smooth aluminium plate (AL) of dimensions 400 mm (length) X 300 mm (width) X 5 mm (thickness) was used for studying the shear response through AE. The roughness of the PLA, GM and ST was determined using a stylus profilometer over an evaluation length of 4 mm. The average roughness (R_a) of PLA was found to be 28–32 µm, and that of GM was 2–3 µm, while the R_a of the AL was found to be 0.36 µm.

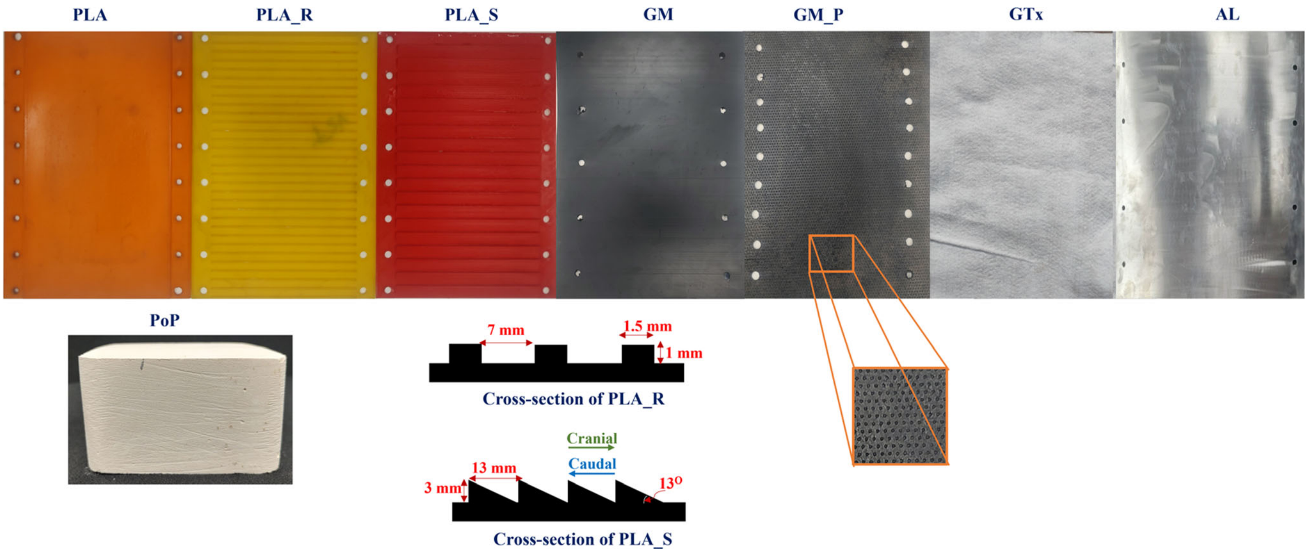

Fig. 5 The continuum surfaces used in the study

3.3 Sample preparation and testing procedure

The sand (QS, GB or AS) was filled and compacted in layers to a relative density of 80% in the shear box kept above the clamped continuum material, as per ASTM D3080 [10]. A suitable gap, as per the particle size, was maintained between the shear box and the continuum surface using spacers during the sample preparation, which were removed just before the commencement of the tests. The CS samples were prepared by compaction in the shear box using custom-made static compaction equipment to maximum dry density with optimum moisture content, the values of which are specified in Table 1. For clay samples, a gap of 1 mm was provided between the shear box and the continuum material by placing a 3D-printed sheet of 1 mm thickness at the bottom of the box before static compaction. Cubes of PoP with dimensions 100 mm X 100 mm X 55 mm were prepared by taking a water content of 60% of the total weight of the mix constituent, as suggested by Sharma et al. [68], and the cubes were cured for 28 days before testing. The edges and sides of the cubes were trimmed appropriately to fit into the shear box. All the samples (QS, GB, AS, CS and PoP) were placed on top of the clamped continuum material, and the intended normal stress was applied on top of the sample. The GTx samples were clamped using a specially designed clamp only at the back edge of the platform, as shown in Fig. 6, so that a pull-out force is exerted when the platform is pulled backwards using the stepper motor. Some QS particles were coloured to obtain texture for the DIC, while the GTx was spray-painted for texturing. A displacement rate of 1 mm/min, as per ASTM D5321 [14], was adopted in all the interface shear tests, except for the continuum–continuum (PoP–PLA_S) interface shear tests, where a higher displacement rate of 9 mm/min was adopted to simulate the requirement of the intended application.

All the sensors used in the apparatus, namely the horizontal and vertical LVDTs (ASTM E2309 [17]) and the horizontal and vertical load cells (ASTM E4 [16]), were calibrated before the tests. For the acoustic emission studies, the Hsu–Nielsen (H–N) fracture source test, which is also known as a pencil lead breakage (PLB) test, was conducted before every experiment to verify the proper contact between the sensor and the metal plate and the accuracy.

4 Results and discussion

4.1 Repeatability of test results

A series of trials were conducted to ascertain the stability of the apparatus and the repeatability of the test results of the different interfaces. For instance, the shear stress–horizontal displacement responses of the repeatability trials of the QS–PLA and the CS–PLA interfaces at 20 kPa normal stress are presented in Fig. 7a and b, respectively. The close match of the shear stress–horizontal displacement responses of both QS–PLA and CS–PLA interfaces confirms the repeatability of the test results. Further, the statistical analysis of the repeatability test results shown in Fig. 7 is presented in Table 3. Statistically, the repeatability, or the variability in the results of the tests, can be expressed using the coefficient of variation (V), as seen in some studies [22, 30, 69]. The coefficient of variation (V) is defined as:

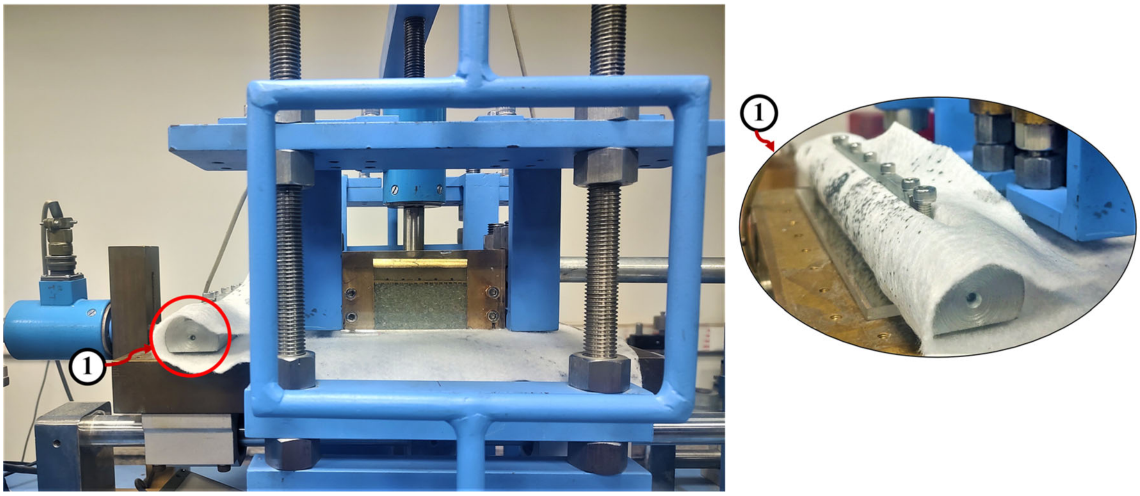

Fig. 6 Clamping arrangement of the GTx for pull-out tests

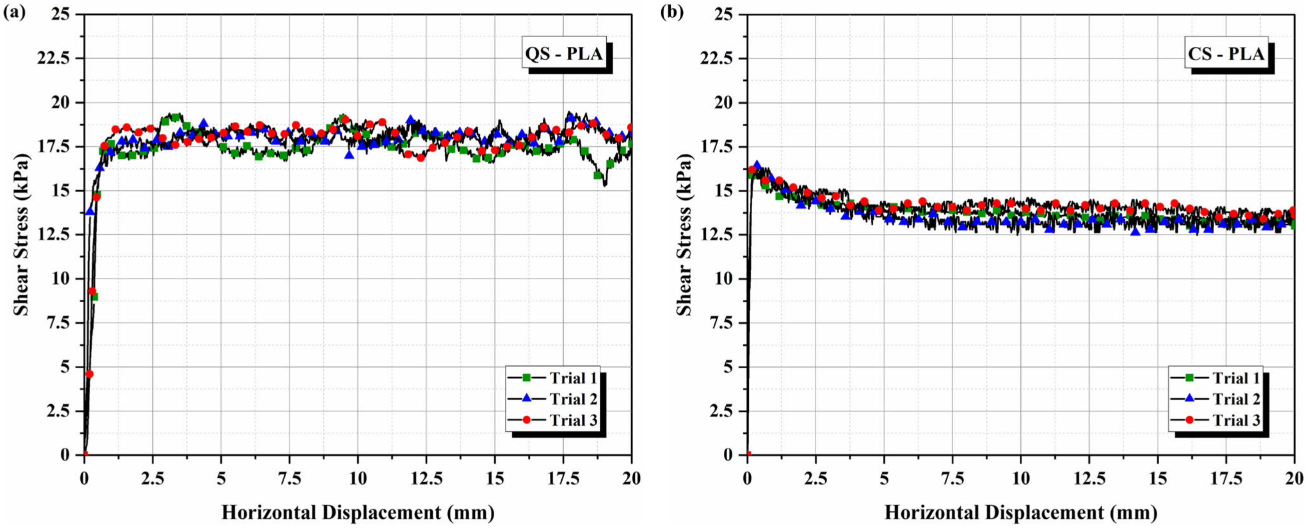

Fig. 7 The repeatability test results of **a** QS–PLA, and **b** CS–PLA

Table 3 Statistical analysis of the repeatability test results

Interface	Trial No	Peak shear stress, kPa	Residual shear stress, kPa	Mean shear stress σ_m, kPa		Standard deviation, X_m		Coefficient of variation (V), %	
				Peak	Residual	Peak	Residual	Peak	Residual
QS–PLA	1	19.40	17.16	19.43	17.80	0.06	0.58	0.30	3.28
	2	19.50	18.30						
	3	19.40	17.95						
CS–PLA	1	16.00	13.33	16.30	13.43	0.30	0.33	1.84	2.47
	2	16.60	13.16						
	3	16.30	13.80						

$$V = \frac{\sigma_m}{X_m} \tag{1}$$

where:

σ_m is the standard deviation of the data,

X_m is the mean of the data.

It can be seen from Table 3 that the V of both interfaces is well within the ranges observed and suggested by Sia and Dixon [15] and Fowmes et al. [30]. Further, the V values are also in agreement with the large data set of interface shear test values presented in Dixon et al. [16], thereby indicating that the accuracy of 1 N of the data acquisition system of the apparatus is sufficient and acceptable. Thus, the newly developed apparatus is capable of producing reliable and repeatable test results for different interfaces.

4.2 Conventional and fixed box configurations

This section presents and discusses the ability and accuracy of the apparatus to accommodate both the conventional and the fixed-box set-up. Interface shear tests were conducted at 20 kPa, 40 kPa and 80 kPa normal stresses with QS–PLA interface, using both fixed box arrangement and the conventional set-up. Figure 8a presents a comparison of the shear stress–horizontal displacement responses of the QS–PLA interface at 20 kPa, 40 kPa and 80 kPa normal stresses for both the fixed box and the conventional conditions, while Fig. 8b presents the corresponding Mohr–Coulomb failure envelopes. It can be seen that the shear stress–horizontal displacement responses are higher in the fixed box condition than in the conventional set-up. The interface friction angle of the fixed box set-up, obtained from the Mohr–Coulomb failure envelope, is 1.6° higher than the conventional set-up. Thus, it appears that the fixed box test set-up slightly overestimates the interface friction angle. The increase in the interface shear stress could be due to the additional stresses that develop along the boundaries of the stationary fixed box, as more sand particles are pressed against them during the shearing. Further, Fig. 9 presents a photograph of the shear box after the interface shear tests of the QS–PLA in both the fixed box (Fig. 9a) and the conventional set-up (Fig. 9b). It can be seen from Fig. 9 that there is a significant rotation of the load plate of about 5° with the centre of the box, or the point of the application of the load in the conventional test set-up, while the rotation of the load plate is negligible in the fixed box condition. It can also be noticed from Fig. 9b that the leading edge of the box is raised 1° higher than the trailing edge. Such a rotation can make the edges of the box in contact with the continuum surface and lead to undesirable stress concentrations. Hence, despite the ease of usage, it is recommended that the conventional set-up be used only in interfaces where significant box rotations are not expected. In other interfaces, such as the continuum–continuum, AE studies, and geotextile pull-out tests reported in the study, the fixed box configuration has been used to simulate the suitable test condition according to the application.

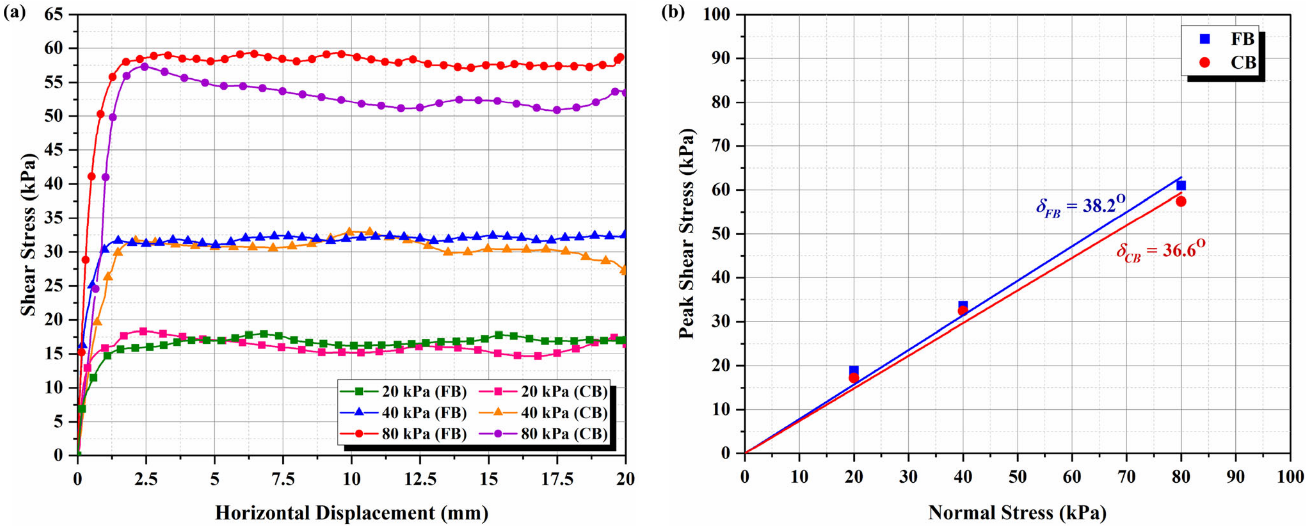

Fig. 8 **a** The shear stress–horizontal displacement responses of QS–PLA in the fixed box (FB) and conventional (CB) test set-ups at 20 kPa, 40 kPa and 80 kPa normal stresses, and **b** the corresponding Mohr–Coulomb failure envelopes

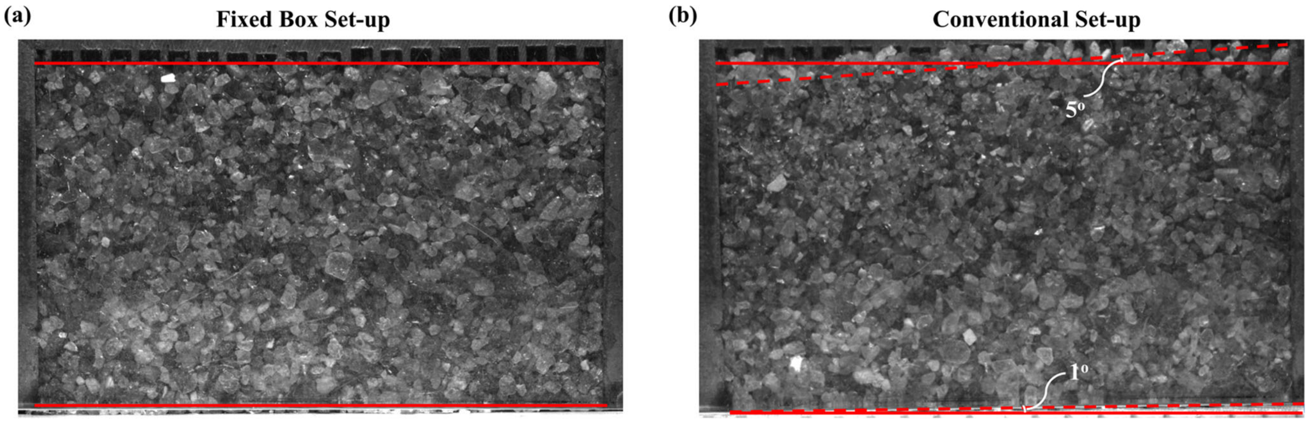

Fig. 9 Photographs showing the shear box at the end of the interface shear tests for **a** fixed box test set-up, and **b** conventional test set-up

4.3 Interface shear tests

4.3.1 Particle–continuum interfaces

This section demonstrates the sensitivity of the apparatus to accurately capture the shear behaviour of the different particle–continuum interfaces. For this purpose, a series of interface shear tests were conducted on several non-dilative (QS–GM, QS–PLA, GB–GM and CS–GM) and dilative (QS–PLA_R and QS–GM_P) interfaces on the apparatus, focussing on different influential parameters such as the shape of the soil particles, the continuum surface properties and the type of the soil. Non-dilative interfaces are those interfaces in which the size of the soil particles is larger than the continuum surface roughness or asperities, while dilative interfaces are those interfaces where the soil particle sizes are small compared to the significant continuum surface roughness [24, 25]. The interface shear responses of the different interfaces are presented as shear stress–horizontal displacement plots, and the interface friction is quantified using the friction angles obtained from the Mohr–Coulomb failure envelopes.

Non-dilative interfaces: Several studies have shown that the shape, or the angularity of the sand particles, influences the shear behaviour of the sand–continuum interfaces [31, 63, 78, 87]. This is particularly true for interfaces where the shearing resistance is predominantly through a ploughing mechanism, such as the non-dilative interfaces between sand and polymeric continuum materials like PLA and GM. These studies point out that the more angular the sand particles are, the higher the interlocking to the continuum and the larger the shear resistance mobilised at the interface. This behaviour is clearly visible from the results of the tests on QS and GB from the apparatus, presented as shear stress–horizontal displacement responses at 20 kPa, 40 kPa and 80 kPa normal stresses for the QS–GM and GB–GM interfaces in Fig. 10a. QS, being more angular than the rounded GB, interlock and establish effective contacts with the continuum surfaces and hence mobilise larger interface shear resistances. As the normal stress increases, the angular particles start ploughing into the continuum surface, which could again result in an increase in the interface frictional resistance. Thus, the interface friction angles of the QS–GM (31.7°) and GB–GM (23.6°) show significant variation, despite the sand particles being the same size, as shown in Fig. 10d.

It is well-established in the literature that the continuum surface roughness [23, 60, 75, 76, 79] is a prominent parameter influencing the shear behaviour of soil–continuum interfaces. These studies have shown that as the surface roughness of the continuum surface increases, the shear resistance at the interface increases, which is also evident from the shear stress–horizontal displacement responses of the QS–PLA and the QS–GM interfaces given in Fig. 10b, and the corresponding failure envelopes. The increase in the interface shear resistance of the QS–PLA compared to the QS–GM can be attributed to the peculiarity of the 3D-printed continuum surfaces. The 3D-printed continuum materials have an additional micro-roughness imposed on their surfaces by the 3D printer itself. The magnitude and extent of the secondary roughness depend on the resolution or accuracy of the 3D printer. The secondary roughness of the PLA results in more resistance to the movement of the soil particles during shear, which results in higher interface frictional resistance in the QS–PLA interface. The interface friction angle of the QS–PLA interface is 15.6% higher than that of the QS–GM interface. Similar results were also observed by Gayathri & Vangla [33], who found that the secondary roughness can indeed have a significant effect on the shear behaviour of soil—3D-printed continuum interfaces, and the effect can be much more prominent for clay interfaces than sand interfaces.

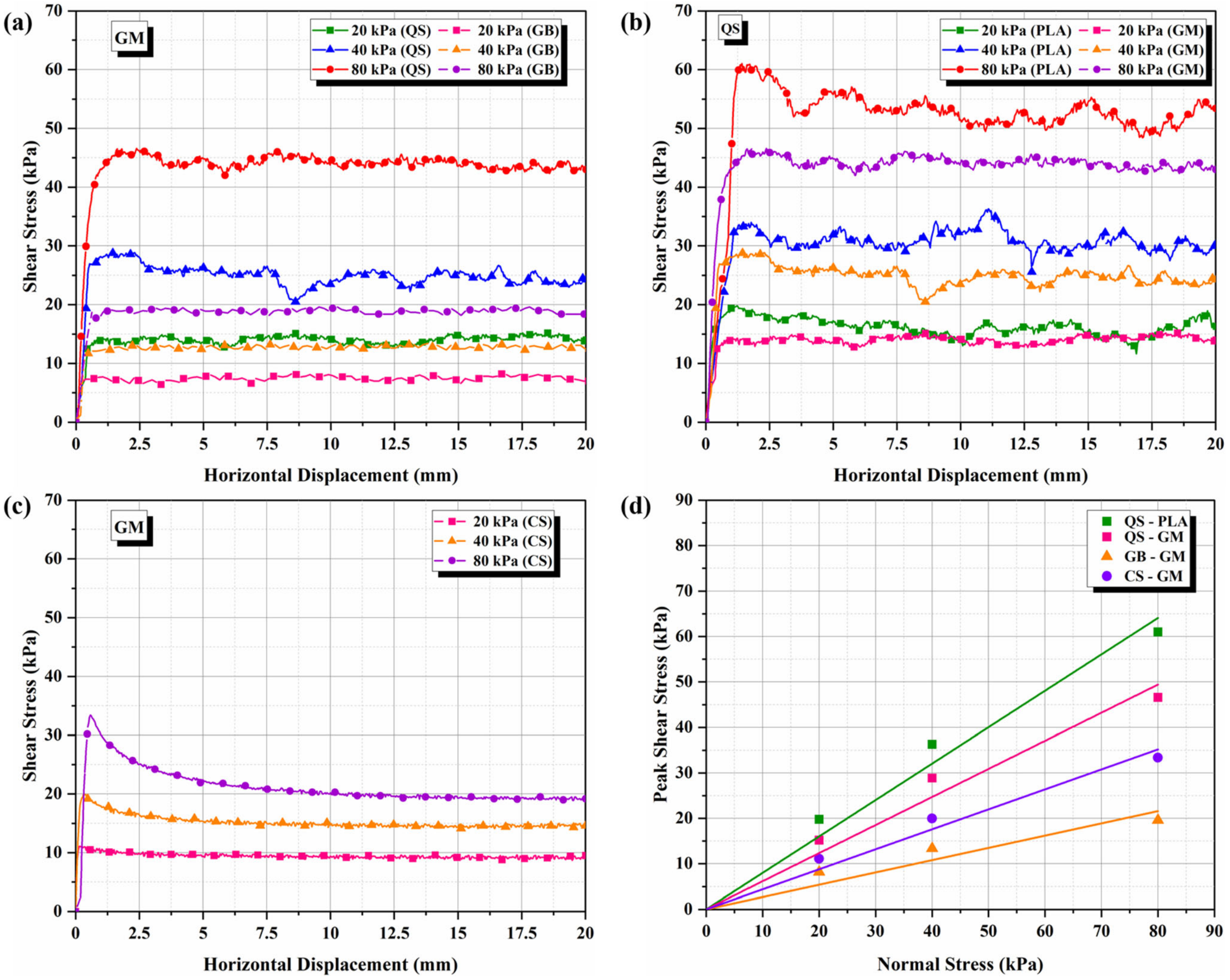

Fig. 10 The shear stress–horizontal displacement responses of **a** QS–GM and GB–GM, **b** QS–PLA and QS–GM, and **c** CS–GM at 20 kPa, 40 kPa and 80 kPa normal stresses, and **d** the Mohr–Coulomb failure envelopes of QS–PLA, QS–GM, GB–GM and CS–GM

The CS–GM interface, as shown in Fig. 10c, shows a different shear response than that of the QS–GM and GB–GM interfaces. The peak shear stresses mobilised by the CS–GM interfaces are smaller than those of the QS–GM and the GB–GM interfaces. The clay sample has a non-discrete cohesive nature, and hence, the shear resistance mobilised at the CS–GM interface is due to a combination of adhesion and sliding along the continuum material, unlike the typical sliding or ploughing of the sand particles. The CS–GM interfaces also exhibit a strain-softening behaviour, which is typical of compacted clay–smooth geomembrane interfaces, as seen from the literature [19, 28, 36].

Dilative Interfaces: Dilative interfaces are the most common interfaces found in geotechnical applications. The increased surface roughness of the continuum materials in the dilative interfaces enhances the frictional properties at the interfaces. Hence, these are widely used in the design of stable and efficient interfaces in geotechnical engineering applications, such as landfill liner systems, deep foundations, mechanically stabilised slopes, retaining walls and soil anchors [3, 4, 72, 74]. The interface shear behaviour of the dilative interfaces in the study is demonstrated using QS–PLA_R and QS–GM_P interfaces.

The shear stress–horizontal displacement responses of QS–PLA_R and QS–GM_P interfaces show significantly different behaviour than their non-dilative counterparts (QS–PLA and QS–GM). Both QS–PLA_R and QS–GM_P interfaces have significantly higher shear stress values, as shown in Fig. 11a. The increase can be attributed to the higher surface roughness of the continuum surface and the associated change in the mechanism of the particle interaction. Both QS–PLA_R and QS–GM_P have surface asperities that cause additional resistance to the motion of the sand particles at the interface, which consequently gives rise to a higher interface frictional resistance. Thus,

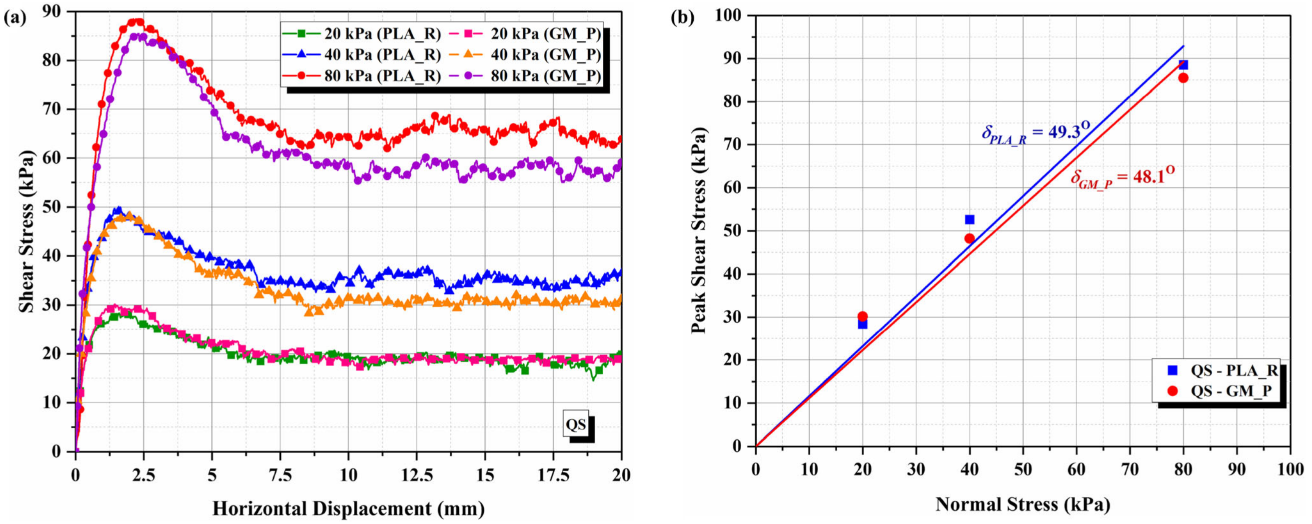

Fig. 11 **a** The shear stress –horizontal displacement response of QS–PLA_R and QS–GM_P interfaces at 20 kPa, 40 kPa and 80 kPa normal stresses, and **b** corresponding Mohr–Coulomb failure envelopes

there is a significant increase in the peak interface friction angles of the dilative interfaces, as shown in Fig. 11b. The higher peak interface friction angles of QS–PLA_R and QS–GM_P also result in efficiency values higher than 1. Efficiency (E) of the interfaces is defined by Koerner [47] as:

$$E = \frac{\tan(\delta_i)}{\tan(\delta_s)} \tag{3}$$

where δ_s is the angle of internal friction of the surrounding soil, and δ_i is the interface friction angle. Efficiency values greater than 1 are common in dilative interfaces [25, 56], especially in ribbed interfaces due to the generation of additional passive resistances [57, 84].

Both QS–PLA_R and QS–GM_P interfaces also exhibit a more prominent strain-softening behaviour than the non-dilative interfaces, as clearly visible from Figs. 10 and 11. Several studies [26, 38, 66] have shown that strain softening in coarse-grained soils is rarely a true material property but rather a result of the inhomogeneous deformation at the shear plane. Both PLA_R and GM_P generate a plane of highly inhomogeneous deformation at the interface due to their high surface roughness and, consequently, cause a significant reduction of post-peak shear strength in the dilative interfaces, unlike the non-dilative interfaces.

A major distinction between the non-dilative and dilative interfaces is their shearing-associated volume changes, as shown in Fig. 12, which shows the vertical

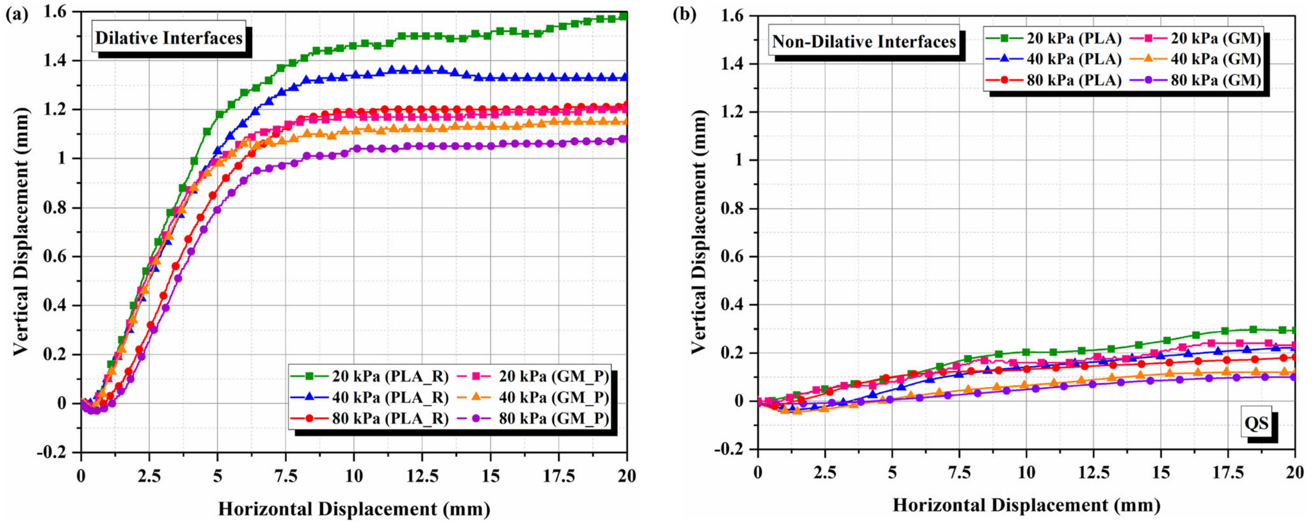

Fig. 12 The vertical displacement–horizontal displacement response of the **a** dilative and **b** non-dilative interfaces

displacement–horizontal displacement plots of the dilative and non-dilative interfaces in Fig. 12a and b, respectively. It can be seen that the vertical displacements are significantly higher in the dilative interfaces than in the non-dilative interfaces, which show negligible volume change during shearing. Non-dilative interfaces have small volume changes at the interface, and the soil above the interfaces does not participate in the shearing process, while dilative interfaces encounter significant volume changes [24, 25] and result in noticeable shear zones. It is also observed that the vertical deformation is lower at higher normal stress due to the constraint exerted by the higher normal stresses. Thus, it is evident that there exists a zone of high deformation at the dilative interfaces, called the shear zone, which can be visualised and analysed using non-contact deformation measurement techniques like DIC, which is further discussed in subsequent sections.

4.3.2 Continuum–continuum interfaces

Recent years have seen the introduction of several innovative interfaces in geotechnical engineering. An example of such an interface is the frictionally anisotropic snakeskin-inspired interfaces [34, 35, 55, 58, 82]. Such interfaces often consist of continuum surfaces with intricate texture or patterns and involve investigating the shearing behaviour between different particulate and continuum materials. This section demonstrates the capability of the apparatus to investigate such complex interfaces. For this purpose, a series of tests are conducted on PLA_S with PoP blocks, which are used to simulate a weak rock mass in the laboratory [68, 82]. The tests were done at higher normal stresses (100 kPa, 200 kPa and 300 kPa).

The peculiarity of a snakeskin-inspired pattern is the direction-dependent frictional resistance, owing to the orientation of the patterns. The patterns have a right-triangular orientation where the hypotenuse rises at an angle of 13° to meet the right side. Thus, two different shearing resistances are developed at the interface depending upon the direction of shearing, with one direction mobilising higher shear stress (cranial) than the other (caudal). The difference in the frictional resistances in the cranial and caudal directions is called frictional anisotropy [37, 59, 67] and can be quantified in terms of the interface friction angles [35]. Figure 13a presents the shear stress–horizontal displacement responses of the PoP–PLA_S interface at 100 kPa, 200 kPa and 300 kPa normal stresses for both cranial and caudal directions, and Fig. 13b presents the corresponding Mohr–Coulomb failure envelopes.

It is clearly evident from Fig. 13a that the shear stress developed in the cranial and caudal directions is vastly different. The cranial direction mobilises significantly higher shear stresses than the caudal direction at all normal stresses and exhibits a significant strain-softening behaviour after a prominent peak. These differences can be attributed to the difference in the interaction of the PoP blocks with the scale angles of the snakeskin-inspired continuum surface. The cranial direction shearing encounters the patterns at a 90° angle, and hence, there is a higher resistance to the shearing than the caudal direction shearing, where the angle is less steep at 13°. The larger resistance in the cranial direction also leads to more wearing of the PoP. The sharp reduction in the post-peak strength in the cranial direction, as shown in Fig. 13a, can be attributed to the sudden drop in the contact points between PoP and PLA_S due to the continuous movement of the continuum surface, leading to larger inhomogeneity

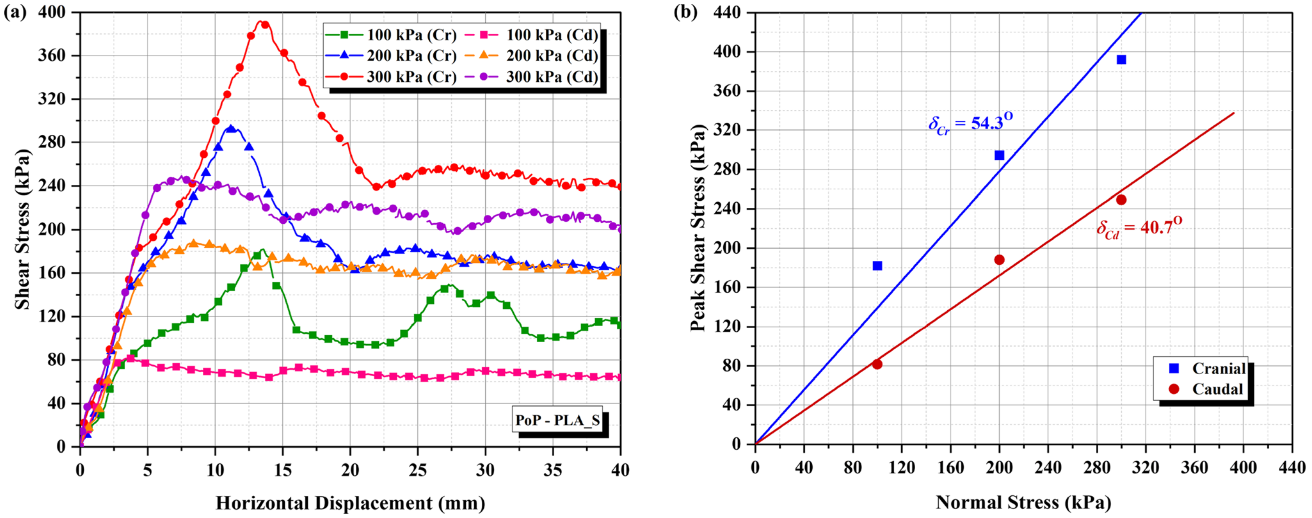

Fig. 13 The shear stress–horizontal displacement response of PoP–PLA_S interface at 20 kPa, 40 kPa and 80 kPa normal stresses for cranial and caudal directions, and **b** corresponding Mohr–Coulomb failure envelopes

and disturbance. These differences lead to a significant frictional anisotropy of 13.6° in the PoP–PLA_S interface, as evident from the Mohr–Coulomb failure envelopes given in Fig. 13b and is significantly higher than the frictional anisotropy observed in snakeskin-inspired patterns and sand interfaces [35, 58].

4.4 Image analysis capabilities

4.4.1 Visualisation and analysis of shear zones

Digital image correlation (DIC) is an excellent and promising tool to analyse and visualise the non-uniformities in the stresses and strains at the interface in a direct shear test set-up. The visualisation and analysis of shear zones in a soil–continuum interface, particularly a dilative interface, are of prime importance for the complete understanding of their peak and post-peak shear response. The development of the shear zones of QS–PLA_R interfaces is analysed using the images captured throughout the shearing process to demonstrate the capability of the apparatus to accommodate DIC for the visualisation of the shear zones. To this end, the DIC analysis of the tests on the QS–PLA_R interface is carried out for the peak shear stress condition and at 8 mm horizontal displacement, which is where the shear stress reaches a constant value and the shear bands may be developed completely, for both 20 kPa and 80 kPa normal stresses, as observed in Fig. 11. The images captured using the CMOS cameras from the side of the shear box were converted to grey-scale and analysed using Ncorr, which is an open-source 2D Digital Image Correlation (2D-DIC) MATLAB software [18]. The images used in the DIC analysis were found to have a resolution of 25 pixels/mm, or 37.5 pixels/grain. The horizontal deformation colour maps of the QS–PLA_R interface at 20 kPa and 80 kPa normal stresses at the peak shear stress are given in Fig. 14a and d, respectively, while the same at 8 mm horizontal displacement of the platform is given in Fig. 14b and e, respectively.

It can be seen from Fig. 14a and d that at the peak, thin and almost horizontal shear bands have developed exclusively at the interface, with minimal soil deformation occurring above these shear bands, for both normal stresses. This pattern indicates a quasi-simple shear mode of deformation, as reported by Shibuya et al. 1997. However, it can be seen from Fig. 14b and e that there exists a zone of high horizontal deformation, known as the shear zone, at the interface, at both the normal stresses at 8 mm displacement. The soil above these zones has shown some horizontal displacements, which may indicate the development of non-uniform strains in the sample after the peak. These observations are aligned with the image analysis results of Vangla and Gali [77], who demonstrated that the independent rotation of the soil sample and shear box in the conventional shear box arrangement while shearing induces some deformation in the soil above the shear zones at the interface after achieving the peak shear stress. Vangla and Gali [77] also observed that the conventional shear box arrangement and symmetric loading arrangement (as suggested by Jewell [43]) yield similar peak shear stress responses with minimal variations in post-peak response for dilative interfaces compared to the fixed box arrangement. However, the shear responses of non-dilative interfaces remain unaffected by the fixity or arrangements of the shear box. These findings suggest that non-uniform strains are mainly observed after achieving peak shear stress in the conventional shear box arrangement for dilative interfaces and are evident from the DIC analysis of the QS–PLA_R interfaces as well. It is also clear from Fig. 14b and e that there are comparatively larger deformations of the QS particles at 20 kPa normal stress than at 80 kPa normal stress. The thickness of the shear zone is also higher at 20 kPa normal stress than at 80 kPa normal stress. It is interesting to note that the fully developed shear zones in Fig. 14b and e are not horizontal throughout the length of the sample and vary from thinner at the edges of the sample to thicker at the centre. At the edges, the shear zone is, in fact, in the form of a slanting plane, as observed in [41, 62] and could be due to the boundary effects exerted by the sides of the shear box on the sand samples.

The quantitative insights into the shear-induced deformation and the shear zones of sand–continuum interfaces the horizontal displacement values of the QS–PLA_R interface, as obtained from the DIC analysis of the shear tests at 20 kPa and 80 kPa normal stresses, for the entire sample height are compared to assess the shear zone thickness, as shown in Fig. 14c and f. The average horizontal displacements at the centre of the shear box are considered in the figure as these are free from the boundary wall effects.

It is clear from Fig. 14c and f that the thickness of the shear zone is higher at 20 kPa normal stress than at 80 kPa normal stress and is 17 mm, which is approximately 11 times D_{50} of QS. On the other hand, the shear zone thickness at 80 kPa normal stress is 11 mm or approximately 7 times D_{50}. It is also clear that the magnitude of the total horizontal displacement of the QS particles is higher at 20 kPa normal stress than at 80 kPa normal stress throughout the shear zone. Figure 14c and f also shows the negligible value of deformation that occurs at the peak shear stresses at both 20 kPa and 80 kPa normal stresses.

Thus, the DIC analysis of the shear zones proves the confinement effect of the higher normal stresses that constrict the movement of the sand particles, consequently reducing the dilation of the sand at the interface, in addition to acting as a tool to visualise the progression and

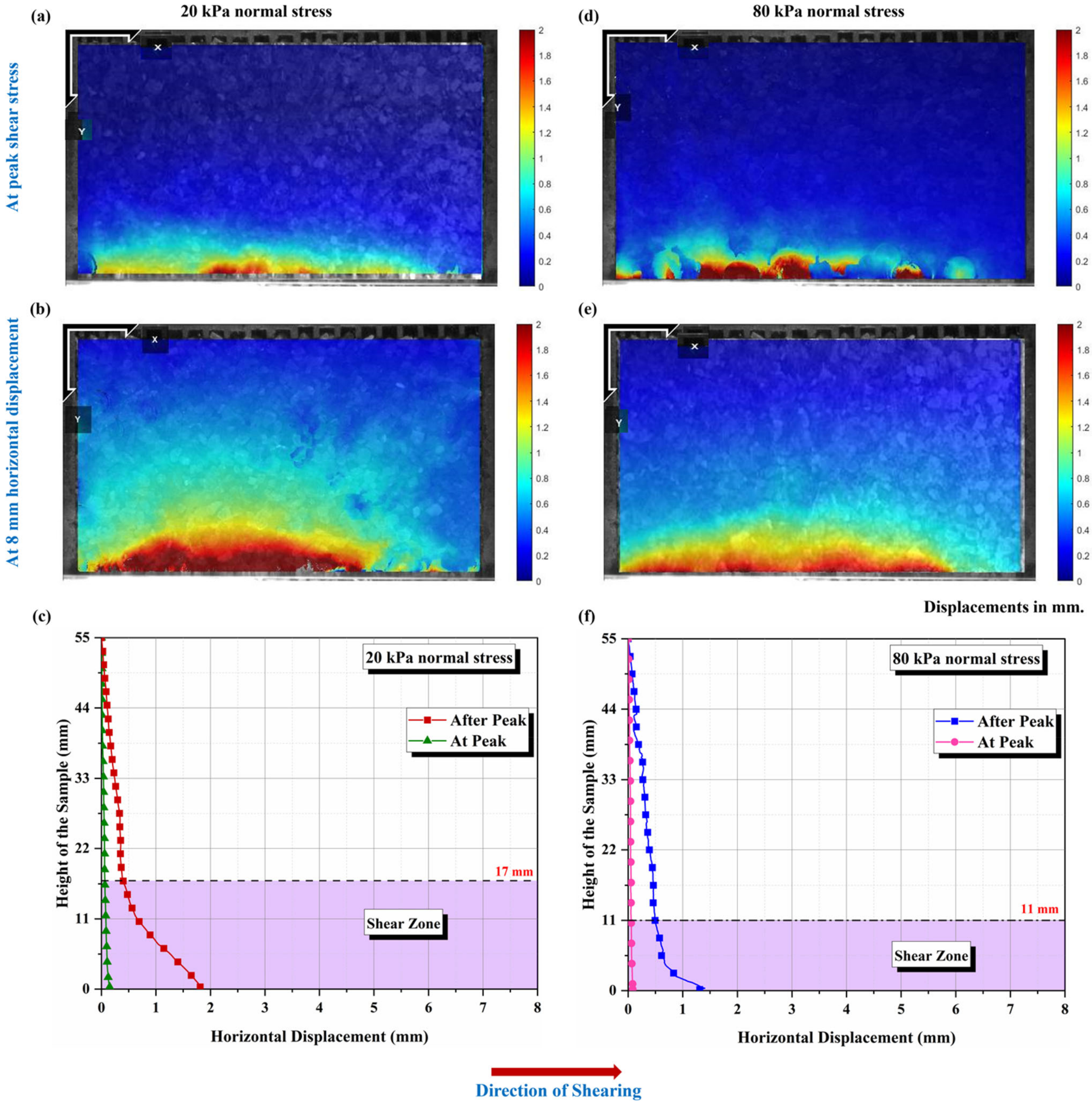

Fig. 14 The horizontal deformation colour maps of QS–PLA_R interface at peak shear stress for **a** 20 kPa normal stress, at 8 mm horizontal displacement for **b** 20 kPa normal stress, and **e** 80 kPa normal stress; the horizontal displacements at the centre of the samples at peak shear stress and at 8 mm displacement for **c** 20 kPa normal stress, and **f** 80 kPa normal stress

development of shear zones as the shearing progresses and quantitatively measure the soil deformation and thickness of the shear zone. The use of DIC to arrive at a quantitative understanding of the shear behaviour of dilative soil–continuum interfaces has also been demonstrated by Gayathri & Vangla [32] and those of non-dilative interfaces by Kandpal & Vangla [45].

4.4.2 Visualisation and analysis of geotextile elongation

Interface pull-out shear tests are conducted for the AS–GTx interfaces at 25 kPa, 50 kPa and 100 kPa to demonstrate the ability of the apparatus to capture and visualise the deformation of the entire shearing area from the bottom of the sample and not only at discrete locations. The shear stress–horizontal displacement responses of the AS–GTx interfaces show a strain-hardening behaviour up to 30 mm

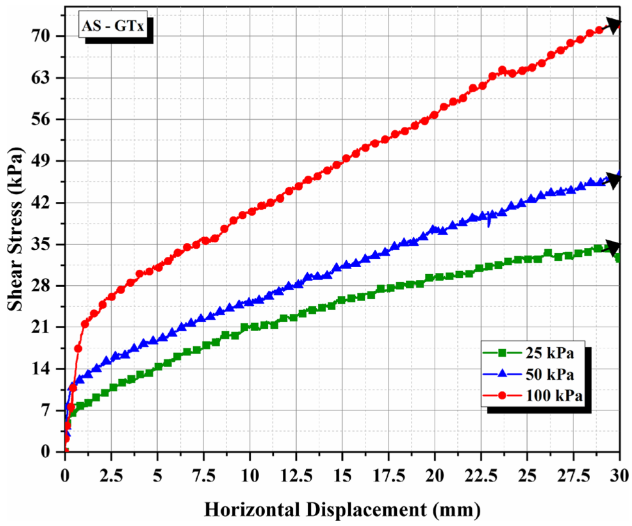

Fig. 15 The shear stress–horizontal displacement behaviour of AS–GTx interface

horizontal displacement, as shown in Fig. 15. For the range of horizontal displacement considered (i.e. up to 30 mm), such a strain-hardening behaviour has also been observed by several studies [2, 53] and may indicate that a full-failure of the geotextile fibres has not taken place. However, the initial pull-out response, which is critical for analysing the various modulus, Hookean and non-Hookean regions of the geotextile, was captured. Further, analysis through DIC was carried out to get more insights into the shear response at this region, the results of which are presented below.

The results of the DIC analysis of the interface pull-out tests for the area of contact of the sand inside the shear box and the geotextile at 30 mm horizontal displacement, analysed using Ncorr, are shown in Fig. 16. Aiban and Ali [2] noticed that the lateral pressure (or the pull-out stress) is higher at the front wall and drops rapidly with increasing distance from the front wall. Thus, the effect of the pull-out load is not as pronounced at the back edge as at the front edge. This phenomenon is clearly indicated in Fig. 16, which shows that the longitudinal deformation (deformation along the direction of pull-out) is higher at the front wall of the shear box than at the back end at all three normal stresses. This can be attributed to the increase in the area of contact of the soil with the geotextiles from the front wall towards the back wall of the box. It can also be noticed that the lateral deformation (deformation perpendicular to the direction of pull-out) is more at the front corners of the shear box and comparatively uniform for the rest of the box. Both longitudinal and lateral deformations are higher at 25 kPa normal stress and decrease as normal stress increases to 100 kPa. This can be attributed to the confining effect of the higher normal stresses that prevents or restricts the pull-out of the geotextiles.

4.5 Acoustic emission in interface shear tests

To quantify and visualise the recorded acoustic emission, ring down count (RDC) and spectrogram are used. RDC is defined as the number of points the digitally reconstructed waveform of the AE crossed a predefined threshold value, as shown in Fig. 17a. While the RDC shows the AE in the

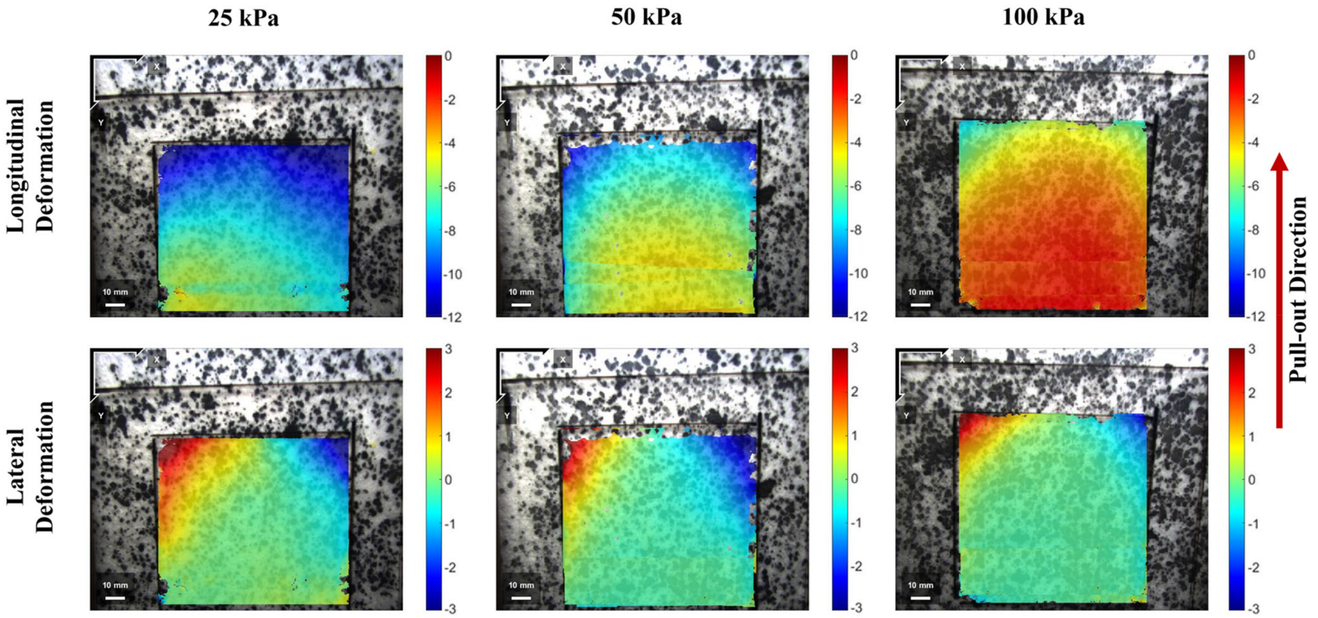

Fig. 16 The longitudinal and lateral displacements of the AS–GTx interface through DIC analysis

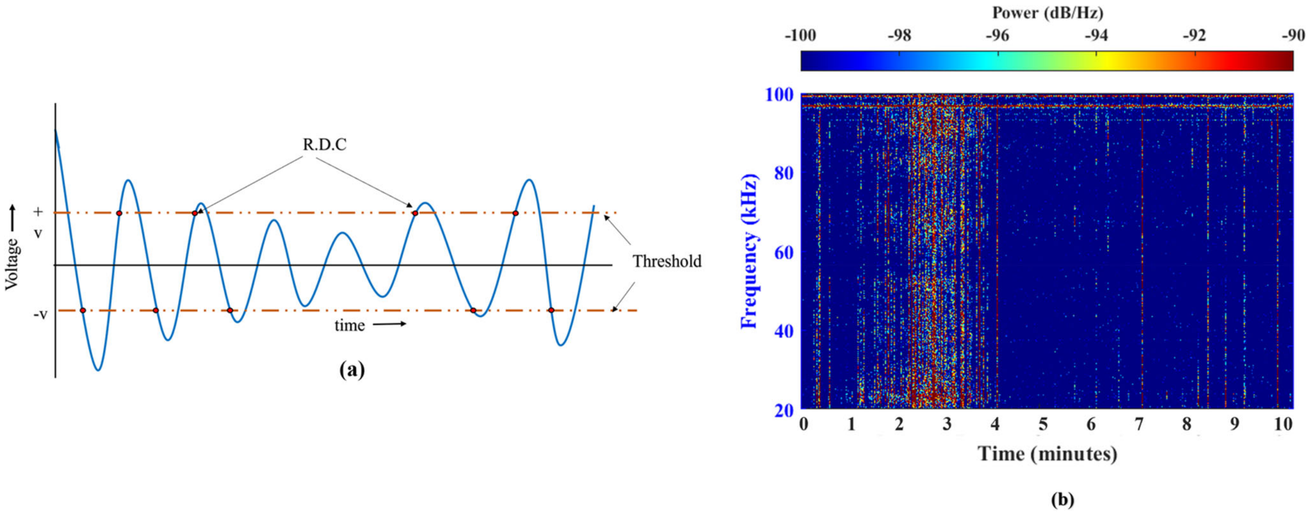

Fig. 17 The schematic depiction of the **a** RDC and **b** spectrogram

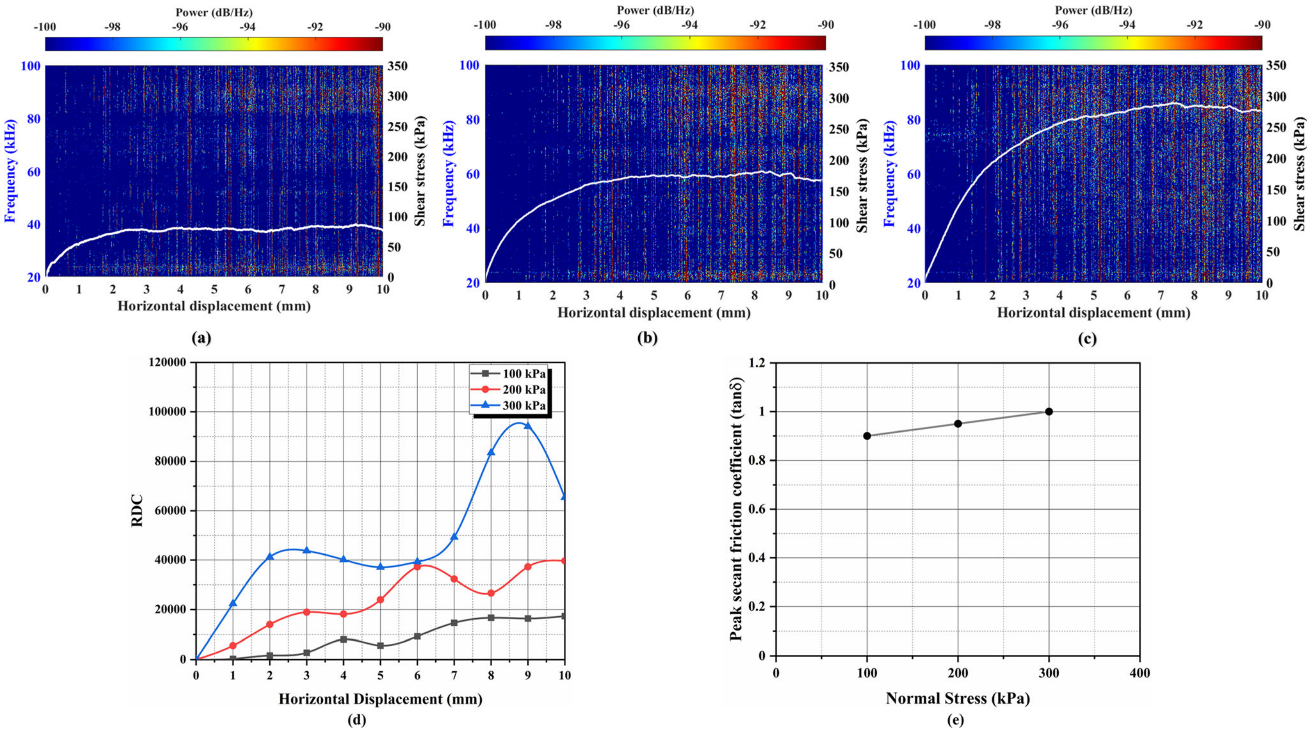

Fig. 18 Shear response of AS-AL interface superimposed on the spectrogram of AE generated during shear at **a** 100 kPa, **b** 200 kPa, and **c** 300 kPa, along with the **d** RDC and **e** tan(δ) vs. σ plot

time domain, a spectrogram is a visual representation of a signal's frequency content over time, displaying how the intensity of various frequencies changes with time using a colour bar, presented in Fig. 17b. The x-axis of the spectrogram typically denotes time, often measured in minutes or seconds. Given that experiments are conducted at a displacement rate of 1 mm/min, the units on the x-axis in spectrograms can be minutes or millimetres (mm). The shear response of the interfaces is superimposed on the spectrogram of the respective AE response to compare and visualise their distribution of the frequencies and intensities.

The AS–AL interfaces were tested under three different normal stresses (100 kPa, 200 kPa, and 300 kPa) in the fixed box configuration to investigate the correlations between the AE and their shear responses. The superimposed plots of interface shear responses on the spectrograms, along with RDC and peak secant friction coefficient

($\tan(\delta)$) vs normal stress (σ) plots, are presented in Fig. 18. With increasing normal stress the peak shear stress increases in all the interfaces as shown in Fig. 18a–c. However, the shear responses exhibit a similar trend where the shear stress increases gradually and becomes plateau with no apparent failure point. Furthermore, the increasing trend in Fig. 18e indicates that the interface failed due to the combined action of ploughing and sliding [24].

The spectrogram shows that the intensities of frequencies increase significantly after the shear stress reaches a plateau or almost constant. In the initial stage, where the increase in shear stress is noticed, no intense bands of AE are observed, as the particles have the least deformations. In the plateau zone, the lower hardness of the aluminium allows particles to plough into the surface, induces additional shearing stress, and maintains almost constant shear stress. This additional stress in the plateau zone causes particle rearrangement [45], resulting in breakage and derailment, generating high AE ranging from 20 to 100 kHz. The AE response in the time domain represented by RDC also supports the hypothesis that a significant increase in the RDC is observed at higher displacement, especially during the plateau zone of the interface shear response. With increasing normal stress peak, RDC increases, establishing a strong correlation between the RDC and the applied normal stress. Hence, the sliding and ploughing of the interfaces can be identified using the AE released by the interface during shearing.

5 Conclusions

The design and functioning of a versatile interface direct shear test apparatus are presented in the paper. The apparatus can support the testing of several particle–continuum as well as continuum–continuum interfaces and can also accommodate different advanced contact and non-contact sensors to gain insights into their interface shear response. The major conclusions drawn from the study are:

- The rotation of the shear box and the loading plate during the interface shear tests can be minimised by adopting the fixed-box configuration. It is recommended that a fixed-box configuration be adopted for interface shear tests where considerable rotation of the shear box is expected or not desired, such as in acoustic emission studies and geotextile pull-out tests.
- The angular particles mobilise higher interface shear stress than the rounded ones, and the sand interface shear response of the clay soil is significantly different than that of the non-dilative interfaces. The presence of the micro-roughness of the PLA also resulted in noticeable changes in the interface shear response of the sand–continuum non-dilative interfaces. The dilative interfaces exhibit significantly different shear stress–horizontal displacement responses than the non-dilative interfaces, with higher interface shear stress values and a post-peak strain-softening. The vertical displacements of the dilative interfaces are also considerably higher than the non-dilative ones. The results confirm the sensitivity of the apparatus to appropriately capture the effect of particle shape, normal stress, type of soil, and the continuum materials on different dilative and non-dilative interfaces. Further, the apparatus produces repeatable test results for different interfaces and the coefficient of variation of the repeatability trials falls well within the reported range.
- The capability of the apparatus to accommodate continuum–continuum interfaces is demonstrated through PoP and an innovative snakeskin-inspired patterned interface. It is observed that the shearing in the cranial direction resulted in a 13.6° increase in the interface frictional angle than shearing in the caudal direction, thus confirming the interface frictional anisotropy of the snakeskin-inspired patterns.
- The DIC analysis of the interface shear tests showed that a shear zone exists at the dilative interface. The thickness of the shear zone reduces as the normal stress increases due to the constraining effect of the normal stress. The provisions in the apparatus to place the camera sensors at the bottom of the sample facilitate novel insights into the pull-out behaviour of geotextiles, and the results showed that the lateral deformation of the geotextile is much lower than the longitudinal deformation, which decreases as the distance from the front wall of the shear box increases. The longitudinal deformation of the geotextiles also decreases as the normal stress increases due to the confining effect of the higher normal stresses that prevents or restricts the pull-out of the geotextiles.
- The provisions of AE in the apparatus can accurately quantify and correlate the AE with the interface shear response, which can pave the way for advanced and insightful interface shear response studies. The RDC and spectrogram of the AE can be used to identify the characteristics of the shear response at various displacements, which can be used to develop AE-based devices to monitor soil–metal interfaces.

The apparatus is a valuable addition to the experimental capabilities of the Indian Institute of Technology Delhi. It can facilitate extensive studies on different interfaces to gain novel and essential insights and acoustic and shear strength parameters.

Acknowledgements This work is supported by the Science and Engineering Research Board (SERB), India (Project code: SRG/2019/

000561). The authors also acknowledge Lt Col Shishir Makwana and Mr Sudeep Nigam, Master of Technology students at the Indian Institute of Technology Delhi, for their assistance.

Data availability The datasets generated and analysed during the current study are available from the corresponding author upon reasonable request.

Declarations

Conflict of interest The authors declare that there is no conflict of interest.

References

1. Abu Qamar MI, Suleiman MT (2023) Development of cyclic interface shear test device and testing procedure to measure the response of cohesive soil-structure interface. Geotech Test J 46:20210270. https://doi.org/10.1520/gtj20210270
2. Aiban SA, Ali SM (2001) Nonwoven geotextile-sabkha and -sand interface friction characteristics using pull-out tests. Geosynth Int 8:193–220. https://doi.org/10.1680/gein.8.0192
3. Airey DW, Kelly RB (2010) Interface behaviours from large diameter ring shear tests. In: Frost JD (ed) Proceedings of the research symposium on characterization and behavior of interfaces. IOS Press, Amsterdam, Netherlands, pp 1–6
4. Alawneh AS, Husein Malkawi AI, Al-Deeky H (1999) Tension tests on smooth and rough model piles in dry sand. Can Geotech J 36:746–753. https://doi.org/10.1139/t98-104
5. Anubhav BPK (2010) Modeling of soil-woven geotextile interface behavior from direct shear test results. Geotext Geomembr 28:403–408. https://doi.org/10.1016/j.geotexmem.2009.12.005
6. Arulrajah A, Rahman MA, Piratheepan J, Bo MW, Imteaz MA (2014) Evaluation of interface shear strength properties of geogrid-reinforced construction and demolition materials using a modified large-scale direct shear testing apparatus. J Mater Civ Eng 26:974–982. https://doi.org/10.1061/(asce)mt.1943-5533.0000897
7. ASTM D698–12 (2021) Standard test methods for laboratory compaction characteristics of soil using standard effort (12, 400 ft-lbf/ft 3 (600 kN-m/m^3)). ASTM Int 3:1–11. https://doi.org/10.1520/D0698-12R21
8. ASTM D854 (2000) Standard test methods for specific gravity of soil solids by water pycnometer. ASTM Int 2458000:1–7. https://doi.org/10.1520/D0854-14
9. ASTM D2487–17 (2017) Standard practice for classification of soils for engineering purposes (unified soil classification system). ASTM Int. https://doi.org/10.1520/D2487-17
10. ASTM D3080 (2011) Standard test method for direct shear test of soils under consolidated drained conditions. ASTM Int. https://doi.org/10.1520/D3080-04
11. ASTM D4253–16 (2016) Standard test methods for maximum index density and unit weight of soils using a vibratory table. ASTM Int 00:1–15. https://doi.org/10.1520/D4253-16E01.1.3
12. ASTM D4254–16 (2016) Standard test methods for minimum index density and unit weight of soils and calculation of relative density. ASTM Int I:9. https://doi.org/10.1520/D4254-16.2
13. ASTM D4318–17 (2005) Standard test methods for liquid limit, plastic limit, and plasticity index of soils. ASTM Int 04:1–14. https://doi.org/10.1520/D4318-17
14. ASTM D5321 (2021) Standard test method for determining the shear strength of soil-geosynthetic and geosynthetic-geosynthetic interfaces by direct shear. ASTM Int. https://doi.org/10.1520/D5321
15. ASTM D5321, D5321M-21 (2021) Standard test method for determining the shear strength of soil-geosynthetic and geosynthetic-geosynthetic interfaces by direct shear. ASTM Int. https://doi.org/10.1520/D5321_D5321M-21
16. ASTM E4 (2021) Standard practices for force calibration and verification of testing machines. ASTM Int. https://doi.org/10.1520/E0004-21
17. ASTM E2309, E2309M (2020) Standard practices for verification of displacement measuring systems and devices used in material testing machines. ASTM Int. https://doi.org/10.1520/E2309_E2309M-20
18. Blaber J, Adair B, Antoniou A (2015) Ncorr: open-source 2D digital image correlation matlab software. Exp Mech 55:1105–1122. https://doi.org/10.1007/s11340-015-0009-1
19. Byrne RJ, Kendall J, Brown S (1992) Cause and mechanism of failure Kettleman Hills landfill B-19, phase IA. In: Stability and performance of slopes and embankments II. ASCE, pp 1188–1215
20. Choo CS, Ong DEL (2015) Evaluation of pipe-jacking forces based on direct shear testing of reconstituted tunneling rock spoils. J Geotech Geoenviron Eng. https://doi.org/10.1061/(ASCE)GT.1943-5606.0001348
21. Chu L-M, Yin J-H (2005) Comparison of interface shear strength of soil nails measured by both direct shear box tests and pullout tests. J Geotech Geoenviron Eng 131:1097–1107. https://doi.org/10.1061/(asce)1090-0241(2005)131:9(1097)
22. Dixon N, Jones DRV, Fowmes GJ (2006) Interface shear strength variability and its use in reliability-based landfill stability analysis. Geosynth Int 13:1–14. https://doi.org/10.1680/gein.2006.13.1.1
23. Dove JE, Frost JD (1996) A method for measuring geomembrane surface roughness. Geosynth Int 3:369–392. https://doi.org/10.1680/gein.3.0067
24. Dove JE, Frost JD (1999) Peak friction behavior of smooth geomembrane-particle interfaces. J Geotech Geoenviron Eng 125:544–555. https://doi.org/10.1061/(ASCE)1090-0241(1999)125:7(544)
25. Dove JE, Jarrett JB (2002) Behavior of dilative sand interfaces in a geotribology framework. J Geotech Geoenviron Eng 128:25–37. https://doi.org/10.1061/(ASCE)1090-0241(2002)128:1(25)
26. Drescher A, Vardoulakis I (1982) Geometric softening in triaxial tests on granular material. Geotechnique 32:291–303. https://doi.org/10.1680/geot.1982.32.4.291
27. Dyer MR (1985) Observation of the stress distribution in crushed glass with applications to soil reinforcement. University of Oxford, Oxford
28. Esterhuizen JJB, Filz GM, Duncan JM (2001) Constitutive behavior of geosynthetic interfaces. J Geotech Geoenviron Eng 127:834–840. https://doi.org/10.1061/(ASCE)1090-0241(2001)127:10(834)
29. Feng SJ, Shen Y, Zheng QT, Shi JL (2022) Multi-functional direct shear apparatus for geosynthetic interfaces with its application on various GMB/GCL interfaces. Acta Geotech 17:993–1008. https://doi.org/10.1007/s11440-021-01279-6
30. Fowmes GJ, Dixon N, Fu L, Zaharescu CA (2017) Rapid prototyping of geosynthetic interfaces: Investigation of peak strength using direct shear tests. Geotext Geomembr 45:674–687. https://doi.org/10.1016/j.geotexmem.2017.08.009
31. Frost JD, Kim D, Lee S (2012) Microscale geomembrane-granular material interactions. KSCE J Civ Eng 16:79–92. https://doi.org/10.1007/s12205-012-1476-x

32. Fuggle AR (2011) Geomaterial gradation influences on interface shear behavior. (Doctoral Dissertation), Georgia Institute of Technology, Atlanta, USA
33. Gayathri VL, Vangla P (2023) Experimental investigation of the suitability of 3D printing for soil-continuum interface studies. Geo-congress 2023. American Society of Civil Engineers, Reston, VA, pp 497–506
34. Gayathri VL, Vangla P (2023) Shear behaviour of snakeskin-inspired ribs and soil interfaces. Acta Geotech. https://doi.org/10.1007/s11440-023-02009-w
35. Gayathri VL, Vangla P, Riya A (2022) Effect of snakeskin-inspired patterns on the shear response of soil—continuum interfaces. Int J Geotech Eng 16:759–775. https://doi.org/10.1080/19386362.2022.2066049
36. Gilbert RB, Byrne RJ (1996) Strain-softening behavior of waste containment system interfaces. Geosynth Int 3:181–203. https://doi.org/10.1680/gein.3.0059
37. Hazel J, Stone M, Grace MS, Tsukruk VV (1999) Nanoscale design of snake skin for reptation locomotions via friction anisotropy. J Biomech 32:477–484. https://doi.org/10.1016/s0021-9290(99)00013-5
38. Hettler A, Vardoulakis I (1984) Behaviour of dry sand tested in a large triaxial apparatus. Geotechnique 34:183–197. https://doi.org/10.1680/geot.1984.34.2.183
39. Hryciw RD, Irsyam M (1993) Behavior of sand particles around rigid ribbed inclusions during shear. Jpn Soc Soil Mech Found Eng 33:1–13
40. Huang L, Martinez A (2020) Study of interface frictional anisotropy at bioinspired soil-structure interfaces with compliant asperities. Geo-congress 2020: biogeotechnics. American Society of Civil Engineers Reston, VA, pp 253–261
41. Indraratna B, Ngo NT, Rujikiatkamjorn C, Vinod JS (2014) Behavior of fresh and fouled railway ballast subjected to direct shear testing: discrete element simulation. Int J Geomech 14:34–44. https://doi.org/10.1061/(ASCE)GM.1943-5622.0000264
42. Irsyam M, Hryciw RD (1991) Friction and passive resistance in soil reinforced by plane ribbed inclusions. Geotechnique 41:485–498. https://doi.org/10.1680/geot.1991.41.4.485
43. Jewell RA (1989) Direct shear tests on sand. Géotechnique 39:309–322. https://doi.org/10.1680/geot.1989.39.2.309
44. Jewell RA, Wroth CP (1987) Direct shear tests on reinforced sand. Géotechnique 37:53–68. https://doi.org/10.1680/geot.1987.37.1.53
45. Kandpal L, Vangla P (2023) New insights into geotribology of non-dilative interfaces from novel experimental studies. Geosynth Int. https://doi.org/10.1680/jgein.23.00013
46. Khan R, Latha GM (2023) Multi-scale understanding of sand-geosynthetic interface shear response through Micro-CT and shear band analysis. Geotext Geomembr 51:437–453. https://doi.org/10.1016/j.geotexmem.2023.01.006
47. Koerner RM (2005) Designing with geosynthetics. Fifth Pearson Education Inc, New Jersey
48. Lamb H (1917) On waves in an elastic plate. Proc Royal Soc London Ser A Contain Papers Math Phys Char 93:114–128. https://doi.org/10.1098/rspa.1917.0008
49. Lashkari A, Jamali V (2021) Global and local sand–geosynthetic interface behaviour. Geotechnique 71:346–367. https://doi.org/10.1680/jgeot.19.P.109
50. Lee KM, Manjunath VR (2000) Soil-geotextile interface friction by direct shear tests. Can Geotech J 37:238–252. https://doi.org/10.1139/t99-124
51. Lin W, Liu A, Mao W, Koseki J (2020) Acoustic emission behavior of granular soils with various ground conditions in drained triaxial compression tests. Soils Found 60:929–943. https://doi.org/10.1016/j.sandf.2020.06.002
52. Liu SH, Sun D, Matsuoka H (2005) On the interface friction in direct shear test. Comput Geotech 32:317–325. https://doi.org/10.1016/j.compgeo.2005.05.002
53. Lopes ML, Silvano R (2010) Soil/geotextile interface behaviour in direct shear and pullout movements. Geotech Geol Eng 28:791–804. https://doi.org/10.1007/s10706-010-9339-z
54. Maghool F, Arulrajah A, Mirzababaei M, Suksiripattanapong C, Horpibulsuk S (2020) Interface shear strength properties of geogrid-reinforced steel slags using a large-scale direct shear testing apparatus. Geotext Geomembr 48:625–633. https://doi.org/10.1016/j.geotexmem.2020.04.001
55. Martinez A, Dejong J, Akin I, Aleali A, Arson C, Atkinson J, Bandini P, Baser T, Borela R, Boulanger R, Burrall M, Chen Y, Collins C, Cortes D, Dai S, Dejong T, Del Dottore E, Dorgan K, Fragaszy R, Frost JD, Full R, Ghayoomi M, Goldman DI, Gravish N, Guzman IL, Hambleton J, Hawkes E, Helms M, Hu D, Huang L, Huang S, Hunt C, Irschick D, Lin HT, Lingwall B, Marr A, Mazzolai B, Mcinroe B, Murthy T et al (2021) Bio-inspired geotechnical engineering: principles, current work, opportunities and challenges. Géotechnique. https://doi.org/10.1680/jgeot.20.p.170
56. Martinez A, Frost JD (2017) The influence of surface roughness form on the strength of sand—structure interfaces. Geotech Lett 7:104–111. https://doi.org/10.1680/jgele.16.00169
57. Martinez A, Frost JD (2017) The influence of surface roughness form on the strength of sand–structure interfaces. Géotech Lett 7:104–111. https://doi.org/10.1680/jgele.16.00169
58. Martinez A, Palumbo S, Todd BD (2019) Bioinspiration for anisotropic load transfer at soil-structure interfaces. J Geotech Geoenviron Eng 145:04019074-1-04019074–14. https://doi.org/10.1061/(ASCE)GT.1943-5606.0002138
59. Marvi H, Cook JP, Streator JL, Hu DL (2016) Snakes move their scales to increase friction. Biotribology 5:52–60. https://doi.org/10.1016/j.biotri.2015.11.001
60. Paikowsky S, Player C, Connors P (1995) A dual interface apparatus for testing unrestricted friction of soil along solid surfaces. Geotech Test J 18:168–193. https://doi.org/10.1520/GTJ10320J
61. Palmeira EM (1987) The study of soil-reinforcement interaction by means of large scale laboratory tests. University of Oxford, Oxford
62. Peerun MI, Ong DEL, Choo CS (2019) Interpretation of geomaterial behavior during shearing aided by PIV technology. J Mater Civ Eng. https://doi.org/10.1061/(ASCE)MT.1943-5533.0002834
63. Peerun MI, Ong DEL, Choo CS, Cheng WC (2020) Effect of interparticle behavior on the development of soil arching in soil-structure interaction. Tunn Undergr Space Technol 106:103610. https://doi.org/10.1016/j.tust.2020.103610
64. Potyondy JG (1961) Skin friction between various soils and construction materials. Géotechnique 11:339–353. https://doi.org/10.1680/geot.1961.11.4.339
65. Powers MC (1953) A new roundness scale for sedimentary particles. J Sediment Res 23:117–119. https://doi.org/10.1306/D4269567-2B26-11D7-8648000102C1865D
66. Read HE, Hegemier GA (1984) Strain softening of rock, soil and concrete—a review article. Mech Mater 3:271–294. https://doi.org/10.1016/0167-6636(84)90028-0
67. Scherge M, Gorb SN, Gorb S (2001) Biological micro-and nanotribology. Springer Science & Business Media, NY
68. Sharma H, Mishra S, Rao KS, Gupta NK (2018) Effect of cover depth on deformation in tunnel lining when subjected to impact load. In: ISRM international symposium–10th asian rock mechanics symposium, ARMS 2018. Singapore

69. Sia AHI, Dixon N (2007) Distribution and variability of interface shear strength and derived parameters. Geotext Geomembr 25:139–154. https://doi.org/10.1016/j.geotexmem.2006.12.003
70. Singh S, Singh G, Prakash C, Ramakrishna S (2020) Current status and future directions of fused filament fabrication. J Manuf Process 55:288–306. https://doi.org/10.1016/j.jmapro.2020.04.049
71. Smith A, Heather-Smith HJ, Dixon N, Flint JA, Pennie D (2020) Acoustic emission generated by granular soil-steel structure interaction. Geotech Lett 10:119–127. https://doi.org/10.1680/jgele.19.00065
72. Stark TD, Williamson TA, Eid HT (1996) HDPE geomembrane/geotextile interface shear strength. J Geotech Eng 122:197–203
73. Thakur V, Nordal S, Viggiani G, Charrier P (2018) Shear bands in undrained plane strain compression of Norwegian quick clays. Can Geotech J 55:45–56. https://doi.org/10.1139/cgj-2016-0443
74. Thenevin I, Blanco-martín L, Hadj-hassen F, Schleifer J, Lubosik Z, Wrana A (2017) Laboratory pull-out tests on fully grouted rock bolts and cable bolts: results and lessons learned. J Rock Mech Geotech Eng 9:843–855. https://doi.org/10.1016/j.jrmge.2017.04.005
75. Uesugi M, Kishida H (1986) Influential factors of friction between steel and dry sands. Soils Found 26:33–46. https://doi.org/10.3208/sandf1972.26.2_33
76. Uesugi M, Kishida H (1986) Frictional resistance at yield between dry sand and mild steel. Soils Found 26:139–149. https://doi.org/10.3208/sandf1972.26.4_139
77. Vangla P, Gali ML (2014) Image-segmentation technique to analyze deformation profiles in different direct shear tests. Geotech Test J. https://doi.org/10.1520/GTJ20130138
78. Vangla P, Gali ML (2016) Shear behavior of sand-smooth geomembrane interfaces through micro-topographical analysis. Geotext Geomembr 44:592–603. https://doi.org/10.1016/j.geotexmem.2016.04.001
79. Vangla P, Gali ML (2016) Effect of particle size of sand and surface asperities of reinforcement on their interface shear behaviour. Geotext Geomembr 44:254–268. https://doi.org/10.1016/j.geotexmem.2015.11.002
80. Vangla P, Latha GM (2015) Influence of particle size on the friction and interfacial shear strength of sands of similar morphology. Int J Geosynth Ground Eng. https://doi.org/10.1007/s40891-014-0008-9
81. Vangla P, Roy N, Gali ML (2018) Image based shape characterization of granular materials and its effect on kinematics of particle motion. Granul Matter. https://doi.org/10.1007/s10035-017-0776-8
82. Vangla P, Wala BA, Gayathri VL, Frost JD (2022) Snakeskin-inspired patterns for frictional anisotropic behaviour of split set rock bolts. Géotech Lett 12:95–100. https://doi.org/10.1680/jgele.21.00076
83. Wang P, Sang Y, Shao L, Guo X (2019) Measurement of the deformation of sand in a plane strain compression experiment using incremental digital image correlation. Acta Geotech 14:547–557. https://doi.org/10.1007/s11440-018-0676-z
84. Wang R, Ong DEL, Peerun MI, Jeng DS (2022) Influence of surface roughness and particle characteristics on soil-structure interactions: a state-of-the-art review. Geosciences (Switzerland) 12:1–36. https://doi.org/10.3390/geosciences12040145
85. Yan X, Gu P (1996) A review of rapid prototyping technologies and systems. CAD Comput Aided Des 28:307–318. https://doi.org/10.1016/0010-4485(95)00035-6
86. Yu M, Reddyhoff T, Dini D, Holmes A, O'Sullivan C (2022) Acoustic emission enabled particle size estimation via low stress-varied axial interface shearing. IEEE Trans Instrum Meas 71:1–10. https://doi.org/10.1109/TIM.2022.3156175
87. Zettler TE, Frost JD, DeJong JT (2000) Shear-induced changes in smooth HDPE geomembrane surface topography. Geosynth Int 7:243–267. https://doi.org/10.1680/gein.7.0174